



Vortex-induced vibration of a circular cylinder on a nonlinear viscoelastic support

Rahul Mishra^{a,b,c,*}, Rajneesh Bhardwaj^b, Salil S. Kulkarni^b, Mark C. Thompson^c

^a IITB-Monash Research Academy, IIT Bombay, Mumbai, 400076, India

^b Department of Mechanical Engineering, IIT Bombay, Mumbai, Maharashtra, 400076, India

^c Fluids Laboratory for Aeronautical and Industrial Research (FLAIR) Department of Mechanical and Aerospace Engineering, Monash University, Clayton 3800, Australia



ARTICLE INFO

Article history:

Received 25 May 2020

Received in revised form 5 November 2020

Accepted 20 November 2020

Available online 7 December 2020

Keywords:

Vortex-induced vibration
Cubic stiffness nonlinearity
Damping
Viscoelasticity

ABSTRACT

The effect of structural nonlinearity on vortex-induced vibration of a rigid circular cylinder has been studied computationally for a fixed mass ratio of $m^* = 2.546$ at $Re = 150$. The arrangement of the springs and damper is similar to setup for the *Standard Linear Solid* (SLS) model used to model a viscoelastic material. One linear spring is in series with the damper and another nonlinear spring is parallel with the damper. The nonlinear structural system is governed by the following three parameters: (a) the ratio of the linear spring constants (R), (b) damping ratio (ζ), and (c) nonlinearity strength (λ). The focus of the present study is to examine the response of the cylinder to VIV by changing ζ and λ . The peak amplitude decreases in comparison with a linear spring, as spring softening ($\lambda < 0$) is increased; in contrast, the peak amplitude increases for a hardening spring ($\lambda > 0$). The equivalent reduced velocity (U_r^{eq}), a measure of nonlinearity, is affected by damping, showing the non-monotonic variation with ζ . There exists a critical value $\zeta \approx 1$ below which the equivalent reduced velocity decreases and beyond which U_r^{eq} increases. We also observed at high values of λ (e.g. $\lambda = 4$), the peak lift force coefficient is almost constant over a wide range of reduced velocity, with the absence of the lower branch for a very low ($\zeta = 0.001$) and high ($\zeta = 10$) values of damping. This near constant amplitude range suggests a hardening spring may be useful for extending the operational range for energy extraction applications. Finally, increased system nonlinearity leads to considerably richer spectral content in the displacement and force signals, reflected in the wake development.

© 2020 Elsevier Ltd. All rights reserved.

1. Introduction

Vortex-induced vibration (VIV) occurs when the shedding of vortices (generally in the form of a von Kármán vortex street) exerts an oscillatory cross-stream force on a cylinder. In particular, elastic structures with a natural structural frequency close to the forcing frequency may develop large-amplitude flow-induced oscillations by extracting energy from the flow. The VIV response of a circular cylinder in uniform flow is determined by the Reynolds number, the mass ratio, the damping ratio, and the reduced velocity. The Reynolds number is defined as $Re = U_\infty D \nu$, where U_∞ is the free stream velocity, D is the cylinder diameter and ν is the kinematic viscosity of the fluid. The mass ratio is defined as

* Corresponding author at: IITB-Monash Research Academy, IIT Bombay, Mumbai, 400076, India.
E-mail address: rahulmishra.iitk@gmail.com (R. Mishra).

Nomenclature

λ	Nonlinearity strength ($= D/\sqrt{k/a}$ for hardening spring) and ($= -D/\sqrt{-k/a}$ for softening spring)
ν	Kinematic viscosity of the fluid
ρ	Fluid density
ζ	Damping ratio
a	Strength of the cubic stiffness nonlinearity
$A_{y,max}^*$	Maximum amplitude of cylinder oscillation
c	Damping coefficient
C_L	Lift force along transverse direction ($= 2F_y/\rho DU_\infty^2$)
D	Cylinder diameter $D = 1$
f_n	Structural natural frequency based on k (undamped) ($= \sqrt{k/m}$)
f_v	Vortex shedding frequency of a non-oscillating cylinder
f_y	Transverse oscillation frequency of cylinder
f_{ls}	Structural natural frequency of linear system consists of k, k_n, c
f_s	Structural natural frequency of nonlinear system consists of $(k, a), k_n, c$
k	Equilibrium stiffness of the spring
k_n	Non Equilibrium stiffness of the spring
L	Spanwise length of cylinder
m	Mass per unit length of cylinder
m^*	Mass ratio ($= 4m/\pi \rho D^2$)
R	Ratio of Non Equilibrium stiffness to Equilibrium stiffness of the spring, k_n/k
Re	Reynolds number ($= U_\infty D/\nu$)
U_∞	Free stream velocity
U_r	Reduced Velocity based on natural frequency of linear part of spring ($= U_\infty/f_n D$)
U_r^{eq}	Equivalent Reduced Velocity based on natural frequency of nonlinear SLS system ($= U_\infty/f_s D$)
<i>Superscript</i> * represents non-dimensional quantity	

$m^* = m/(\pi \rho D^2/4)$ where m and ρ are the mass per unit length and the fluid density, respectively. The damping ratio is given as $\zeta = c/2\sqrt{km}$, where k is the spring stiffness constant.

The problem of vortex-induced vibration of a cylinder, in particular, the case where a rigid circular cylinder is elastically mounted and constrained to oscillate transversely to a free stream, has been well-studied in the literature, as can be seen from comprehensive reviews of [Sarpkaya \(1979\)](#), [Bearman \(1984\)](#), [Parkinson \(1989\)](#), [Sarpkaya \(2004\)](#), [Williamson and Govardhan \(2004, 2008\)](#), [Bearman \(2011\)](#) and [Wu et al. \(2012\)](#). The main features of the problem are summarized below.

Lock-in occurs when the non-dimensional structural period matches the shedding period, typically when $U_r \sim 5$ for a circular cylinder. The reduced velocity range over which the structure undergoes near-resonant vibration is referred to as the lock-in range. The reduced velocity as defined by [Sumer et al. \(2006\)](#) is the ratio of the wavelength of the cylinder trajectory to its diameter is given by $U_r = U_\infty/f_s D$, alternatively, it can be thought of as a non-dimensional structural period. The amplitude of cylinder vibration undergoes jumps as the reduced velocity is changed, which give rise to different branches based on the synchronous response: the upper and lower branches ([Khalak and Williamson, 1999](#)). The combination of the upper and lower branches is called the lock-in region, where the vibration frequency locks onto the natural frequency of the system. The lower branch in higher Re experiments is identified by the lower amplitude of oscillation than the upper branch. The upper and lower branches are also characterized by the phase difference between the lift force and displacement of close to 0° and 180° , respectively.

The current work focuses on VIV of a cylinder mounted on a nonlinear viscoelastic support. The studies on the VIV system with nonlinear restoring forces have shown that such forces can either increase the vibration amplitude and enhance the range of operational flow speeds, with possible application to energy harvesting, or to decrease vibration amplitude when it is undesirable. Notably, [Gammaitoni et al. \(2009\)](#) have used a nonlinear oscillator for energy harvesting, whereas [Lee et al. \(2008\)](#) have used nonlinear oscillator for vibration suppression. [Amabili \(2019\)](#) also investigated nonlinear damping from viscoelasticity by using a single degree-of-freedom model based on the standard linear structural model with geometric nonlinearity inserted in. [Amabili \(2018\)](#) undertook a similar investigation using a fractional viscoelastic standard solid model with geometric nonlinearity. They have both shown experimentally a strong increase in damping with the vibration amplitude during nonlinear vibrations. [Amabili \(2019\)](#) studied the purely structural system with sinusoidal force whereas the current work focused on both, the nonlinear structure and VIV. The current work is aimed at characterizing how VIV is affected when the structural system shows a nonlinear response due to nonlinear viscoelastic support. In addition to this nonlinearity, as for VIV of linear structures, the oscillations modify the wake and

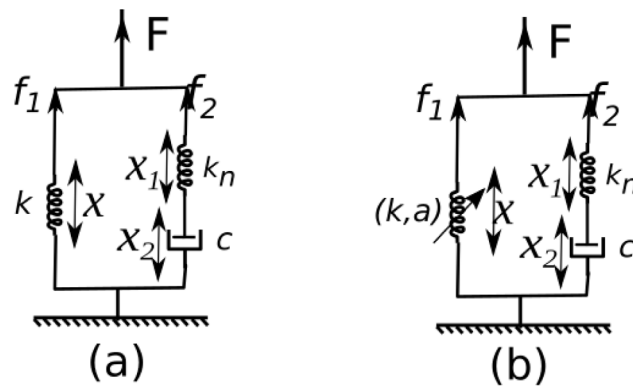


Fig. 1. Schematic of the (a) SLS model with linear springs; (b) Extended SLS model with a nonlinear left spring and linear right spring.

give rise to a nonlinear interaction between the flow and structure. The understanding of the effect of the added structural nonlinearity is of importance to the present study.

The stiffness force of the nonlinear spring is expressed in the form as $f_r = ky + ay^3$. Here k and a denote the linear stiffness and nonlinear cubic stiffness parameters. If a and k both are positive, then the system has only one equilibrium point at $y = 0$, which is stable. This is identified as a hardening system, since the effective stiffness, given by the slope of the restoring force curve, increases with increasing $|y|$. When $k > 0$ and $a < 0$, the system has one stable equilibrium point at $y = 0$ and two unstable equilibrium points at $y = \pm\sqrt{k/|a|}$. In this case, the slope of the restoring force curve decreases with increasing $|y|$, and the system is referred to as softening. If $k < 0$ and $a > 0$, such an oscillator has one unstable equilibrium point at $y = 0$ and two stable equilibrium points at $y = \pm\sqrt{|k|/a}$. This system is referred to as a bistable or double-well oscillator (Badhurshah et al., 2019).

Considerable research has made towards understanding the characteristics of bistable springs. Harne and Wang (2013) has classified the potential methods to induce bistability, such as employing magnetic attraction or repulsion on cantilever structures and imparting mechanical bistability into a piezoelectric structure. They observed an increase in power generation due to large amplitude motion caused by the transition from one stable state to the other. Huynh et al. (2017) have also considered the effects of bi-stable stiffness and hardening stiffness on the performance of VIV systems. They found that bi-stable stiffness allows the system to operate at low-velocity water flows, while the hardening stiffness can extend the operating range for high velocity flows. Mackowski and Williamson (2013) recently verified the nonlinear effect of hardening springs on a VIV system experimentally. From that study, the hardening of the springs was represented through cubic and quintic functions, confirming the possibility of high power efficiency. An alternative form of spring that exhibited hardening was studied experimentally by Huynh et al. (2015). This utilized a cantilever support. Dai et al. (2017) have used nonlinear elements – a nonlinear energy sink (NES) – to absorb vibration in VIV. NES is an essentially nonlinear oscillator that promotes the one-way transfer of energy from the primary structure (the cylinder) to itself. In the present work, we have investigated the effects of both the hardening springs and the softening springs, which may have possible implications for energy extraction.

Previous studies have employed viscoelastic (Findley and Davis, 2013) supported VIV to suppress the vibration induced by vortex shedding. The damping effect on VIV was studied using the Kelvin–Voigt model. In this model, the amplitude response decreases with increasing damping due to an increase in the dissipation of mechanical energy of the cylinder by the damper. de Lima et al. (2018) investigated the effect of viscoelastic-mounting of a cylinder on VIV, examining flow characteristics at $Re = 10000$. They discussed the role of frequency and temperature on viscoelastic properties, and proposed such a viscoelastic support to suppress the vibration induced by vortex shedding. In the current work, we have employed the Standard Linear Solid (SLS) model instead of the Kelvin–Voigt (KV) model, since SLS is a more realistic material model (De Haan and Sluimers, 2001; Findley and Davis, 2013). The Kelvin–Voigt (KV) model is able to describe the creep behaviour but is unable to describe stress relaxation. The SLS model predicts both creep and stress relaxation. More recently, Mishra et al. (2020) investigated the VIV response of a rigid circular cylinder mounted on a viscoelastic support modelled using the Standard Linear Solid (SLS) model. The SLS model consists of one linear spring in series with the damper and another linear spring is parallel with the damper (Fig. 1(a)). They showed that the higher damping ratio ($\zeta > \zeta_c$) response is similar to that at lower damping ratios ($\zeta < \zeta_c$). The non-monotonic vibration amplitude response with damping ratio was shown through a “Griffin Plot”, commonly used to record the amplitude response as the damping ratio is varied. The current paper is an extension of that work to numerically investigate the VIV response of a rigid circular cylinder mounted on a nonlinear viscoelastic support. In this paper, the nonlinear viscoelastic support is modelled as an extended SLS model with a nonlinear spring placed in parallel to a linear spring–damper element Fig. 1(b).

Finally, in relation to the current study, Mishra et al. (2019) used the Standard Linear Solid model (SLS) of viscoelasticity to discuss the response of a viscoelastic thin plate attached to the lee side of the cylinder for $Re = 100$. The tip

displacement amplitude was found to be a non-monotonic function of the structural damping. To the best of the authors' knowledge, VIV of a cylinder mounted on a nonlinear viscoelastic support has so far received little attention in the literature. It is envisaged that such supports can provide an effective means of tuning the nonlinearity for VIV suppression or energy extraction applications.

The paper is organized as follows. In Section 2, the governing equations for the structure, fluid flow, and coupling of the flow and structure solvers are provided. A numerical approach to solve the coupled system is then briefly described. The simulation results are presented in Section 3 as a function of two governing parameters: (a) nonlinearity strength λ ; and (b) damping ratio ζ . The effect of these parameters on the amplitude of vibration, frequency, and lift coefficients is discussed. Finally, the main conclusions of the work are presented in Section 4.

2. Problem definition and methodology

2.1. Governing equations

In the present work, a circular cylinder of diameter D is placed in a free-stream flow. The cylinder is mounted vertically on a viscoelastic support as shown in Fig. 2, and is free to oscillate only in the transverse direction to the flow. The flow is assumed two-dimensional (2D) based on the considered Reynolds number (Re). The fluid is incompressible and viscous, while the motion of the cylinder can be modelled as a spring-mass-damper system shown in Fig. 1. The fluid flow is modelled in the moving reference frame attached to the cylinder. The governing equations are the non-dimensional continuity and Navier–Stokes equations in an accelerated frame of reference, as follows

$$\frac{\partial u_i}{\partial x_i} = 0, \quad (1)$$

$$\frac{\partial u_i}{\partial t} + \frac{\partial u_j u_i}{\partial x_j} = -\frac{\partial p}{\partial x_i} + \frac{1}{Re} \frac{\partial^2 u_i}{\partial x_j^2} + a_i, \quad (2)$$

where u_i and p are the non-dimensional fluid velocity and kinematic pressure, respectively, and a_i is the acceleration of the reference frame attached to the cylinder. The free stream velocity U_∞ and the cylinder diameter D are used as reference scales, respectively.

The coupled fluid–solid system is described by Eqs. (2) and (1), together with the motion of the cylinder in the y -direction governed by the following dimensionless equation (refer to Appendix):

$$\ddot{Y}^* + \frac{R\pi f_n^*}{\zeta} \dot{Y}^* + 4\pi^2 f_n^{*2} (1 + R + 3\lambda^2 Y^{*2}) \dot{Y}^* + \frac{4\pi^3 R f_n^{*3}}{\zeta} Y^* + \frac{4\pi^3 R f_n^{*3} \lambda^2}{\zeta} Y^{*3} = \frac{2R f_n^* C_L}{m^* \zeta} + \frac{2}{\pi m^*} \dot{C}_L \quad (3)$$

where Y^* and C_L correspond to the displacement and hydrodynamic force in the transverse direction. Here, \ddot{Y}^* , \dot{Y}^* , \dot{Y}^* and Y^* are the non-dimensional jerk, acceleration, velocity and displacement of the cylinder respectively. The non-dimensional frequency is given by $f_n^* = Df_n/U_\infty$, where $f_n = \frac{1}{2\pi} \sqrt{k/m}$, $R = k_n/k$, $\zeta = c/2\sqrt{km}$, and m^* is mass ratio defined by $m^* = m/(\pi \rho_f D^2/4)$ per unit spanwise length of the cylinder of length L . In Eq. (3), $C_D = 2F_x/\rho_f U_\infty^2 D$ and $C_L = 2F_y/\rho_f U_\infty^2 D$ are the corresponding drag and lift coefficients per unit length of the cylinder, respectively, where F_x and F_y are the forces exerted on the cylinder in the in-line and transverse directions, respectively. Finally, λ is the nonlinearity strength defined as the inverse of the non-dimensional position at which the force produced by the linear spring is equal to force produced by nonlinearity (Mackowski and Williamson (2013)). For a hardening spring, $\lambda = D/\sqrt{k/a}$, while for a softening spring $\lambda = -D/\sqrt{-k/a}$.

2.2. Numerical approach

The simulations used a non-deformable mesh fixed to the cylinder with an extra non-inertial acceleration term added to the right-hand side of the Navier–Stokes equation (Eq. (2)) to account for the acceleration of the cylinder across the flow. A spectral-element technique is employed for the spatial discretization (Karniadakis and Sherwin, 2013). A detailed implementation of the spectral element method can be found in Thompson et al. (1996), hence a only brief description of the approach is given here.

The spatial domain is discretized into quadrilateral elements. Within each element, the velocity and pressure field, are represented by high-order tensor-product Lagrangian polynomial shape and weighting functions. The node points of these polynomial functions are associated with Gauss–Lobatto–Legendre quadrature integration points. The time integration of the spatially discretized equation was dealt with through a three-step time-splitting scheme that accounts for the advection, pressure, and diffusion terms of Navier–Stokes equation. First, the advection and cylinder acceleration are integrated using the explicit Adams–Bashforth method to update the velocity field. The second step incorporates the effect of the pressure field on the velocity field. This proceeds by taking the divergence of the update step to form a Poisson equation for the pressure forced by the divergence of the velocity field after the advection step. Once the pressure is evaluated through LU decomposition, the intermediate velocity is updated to produce a divergence-free intermediate velocity field. Finally, the diffusion term is incorporated using the Crank–Nicolson scheme to correct the velocity over the timestep. The final step preserves the divergence-free state of the velocity, if it was initially divergence-free at the start of the step. The spectral-element code was recently validated for similar problems by Soti et al. (2017) and Mishra et al. (2020).

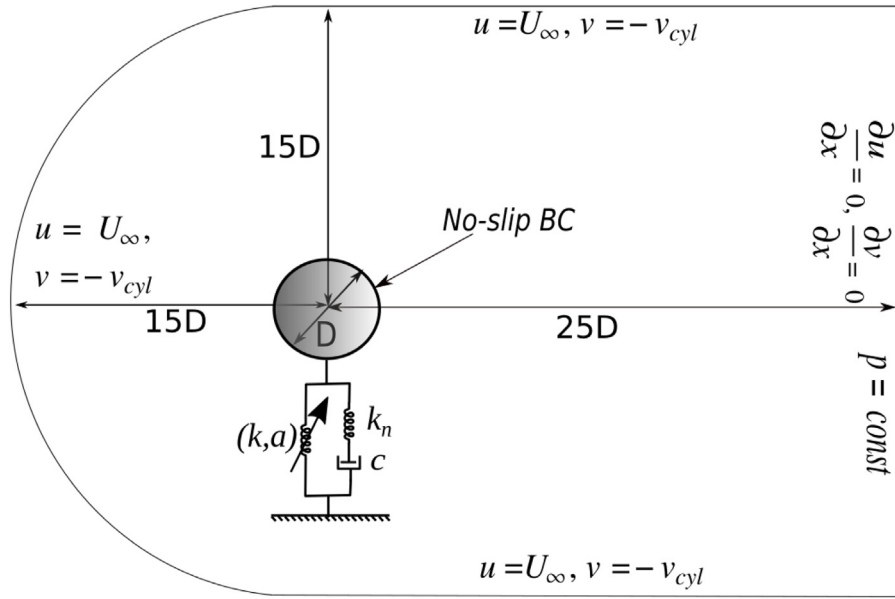


Fig. 2. Schematic of the computational domain and the boundary conditions for the vortex-induced vibration flow problem.

2.3. Computational domain and boundary conditions

A schematic of the computational domain is shown in Fig. 2. The cylinder is constrained to move in the transverse direction to the flow. We use the following parameters: $Re = 150$, and damping ratio $\zeta = [0.001 - 10]$, in the simulations presented hereafter, where Re is based on the cylinder diameter, D , and uniform inflow velocity, U_∞ . The computational domain as shown in Fig. 2, the inlet is a semicircle with a diameter $30D$ and the far-field extends $25D$ downstream. The vibrating cylinder is kept at the centre of the semicircle. The flow boundary conditions are shown in Fig. 2 and are described as follows. The fluid velocity prescribed at the inlet, top, and bottom boundaries is given by $u = U$ and $v = -v_{cyl}$, where u and v are the x and y velocity components, respectively, and v_{cyl} is the cylinder velocity in the absolute frame. At the surface of the cylinder, the no-slip condition is imposed. At the outlet, the normal velocity gradient is set to zero and the pressure is fixed. At no-slip boundaries and at the far-field boundaries, higher-order boundary conditions are used for the pressure gradient (Karniadakis et al., 1991), maintaining mass conservation at boundaries.

2.4. Code validation

The spectral-element implementation has been previously extensively validated against experiments and other codes, e.g., see Hourigan et al. (2001), Sheard et al. (2003), Leontini et al. (2006a) and references therein. This solver has also been used to model closely related vortex-induced vibration problems e.g., for a cylinder: Leontini et al. (2006b,a, 2011); and a sphere: Lee et al. (2013). In addition, for the current simulations, the domain and chosen resolution are based on a previous study of VIV of a circular cylinder for the linear SLS model, where resolution and other validation studies were reported (Mishra et al., 2020).

For the present study, we have undertaken further tests of the implementation of the nonlinear VIV module for a cylinder with a single degree of freedom by considering parameter sets that effectively reduce to the standard elastically mounted cylinder problem. The schematic of the computational domain is shown in Fig. 2, in which the cylinder is mounted on a spring-dashpot viscoelastic model and is free to vibrate only in the transverse direction. The system converts into a linear elastic system for nonlinearity strength $\lambda = 0$. To validate against existing elastic results available in the literature, two viscoelastic cases were considered that reduce to simpler elastic cases: (1) $\zeta = 0$ or $R = 0$; and (2) $\zeta \rightarrow \infty$ for $R = 1$, as depicted in Fig. 3. For $\zeta = 0$, the mounting system acts as single spring with frequency f_1 , whereas for $\zeta \rightarrow \infty$, it act as two springs in parallel with an effective system frequency $f_2 = \sqrt{2}f_1$. The response curves for these cases can be compared with previously reported results from the literature (Bao et al., 2012; Zhao, 2013), and are shown in Fig. 4.

The validation for the nonlinear elastic case is done through a comparison with the numerical results of Wang et al. (2019). The validation case is VIV of a circular cylinder at $Re = 150$, $m^* = 2.546$, and for a non-dimensional frequency $f_n^* = 0.22227$. The nonlinearity strengths considered for two cases were $\lambda = -1.6$ and 4 , the extreme cases for the current study. Fig. 5 shows the comparison of the computed maximum displacement amplitude with the numerical predictions of Wang et al. (2019). There is generally good agreement between two sets of predictions, with slight differences most likely due to differences in the blockage ratio.

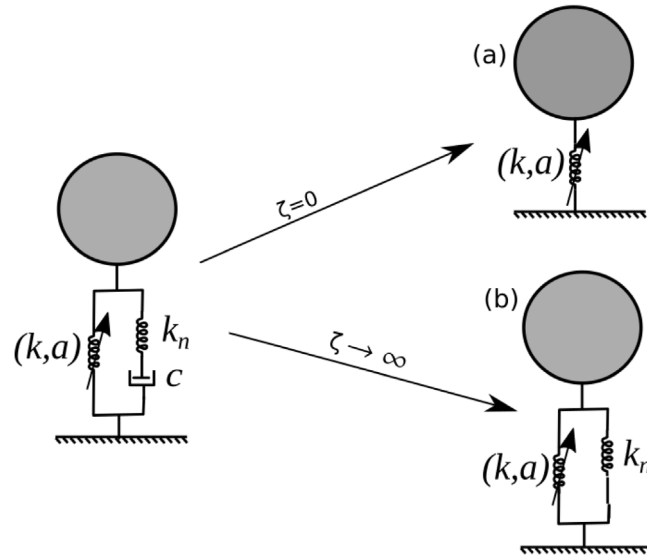


Fig. 3. Schematic of the conversion of the nonlinear viscoelastic system into a nonlinear elastic one: (a) $\zeta = 0$; and (b) $\zeta (= c/2\sqrt{km}) \rightarrow \infty$; for $R(= k_n/k) = 1$. For linear system $a = 0$.

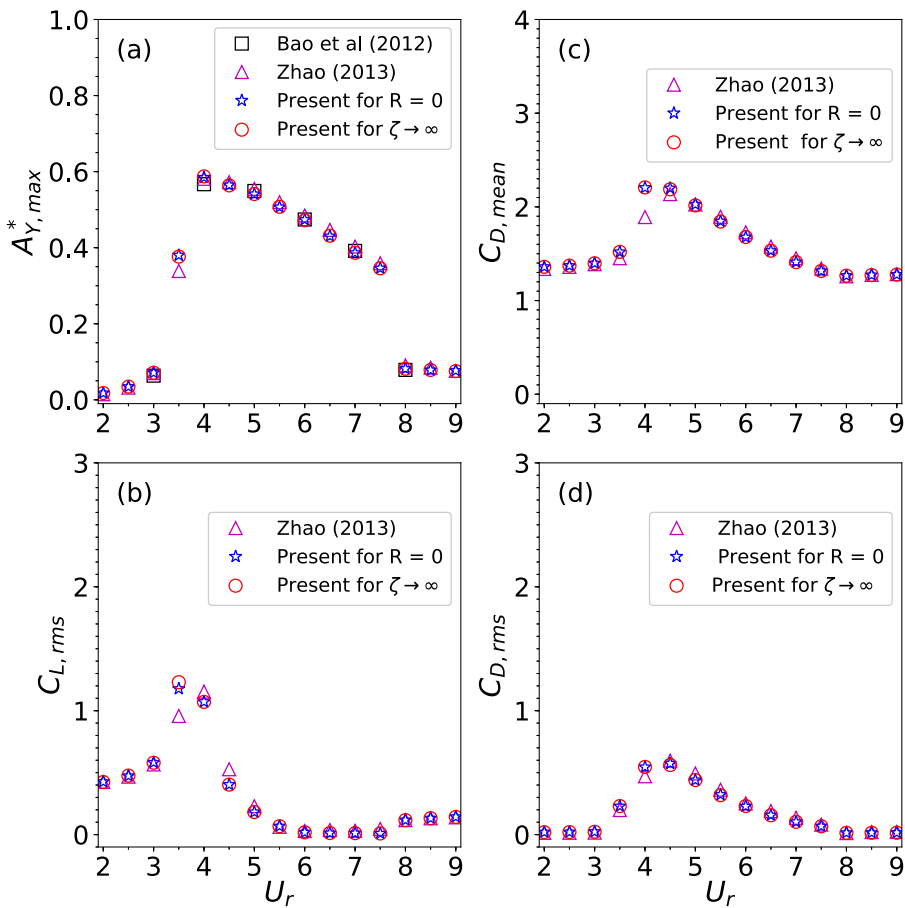


Fig. 4. Comparison of computed (a) Maximum displacement amplitude; (b) Root mean square(RMS) lift coefficients; (c) Mean drag coefficient; (d) RMS drag coefficient; of an undamped cylinder supported on a linear elastic spring undergoing transverse VIV for a linear spring ($\lambda = 0$) with $m^* = 2.546$ (Bao et al., 2012) at $Re = 150$.

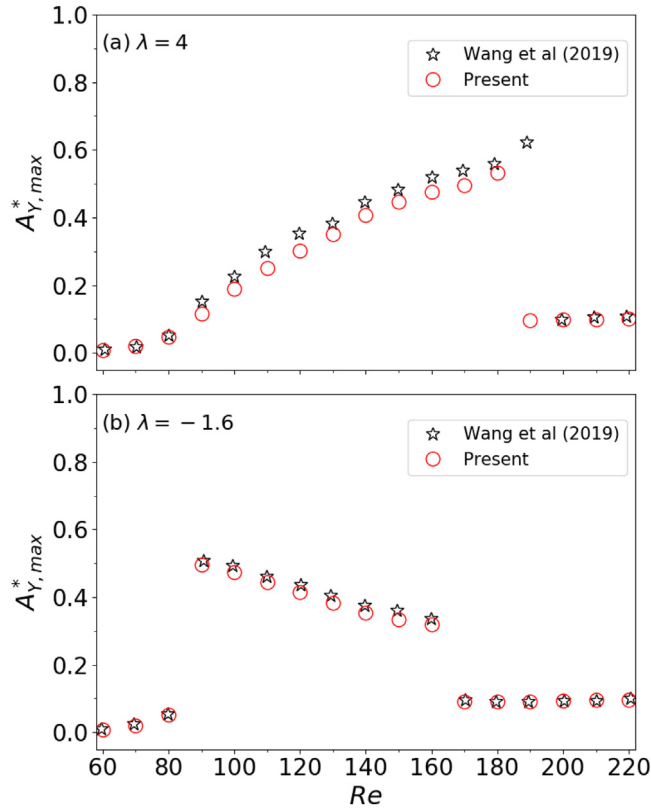


Fig. 5. Comparison of computed maximum displacement amplitude of an undamped cylinder undergoing transverse VIV on nonlinear spring for $m^* = 2.546$, $f_n^* = 0.22227$ at $Re = 150$, (a) $\lambda = 4$, (b) $\lambda = -1.6$ (Wang et al., 2019).

2.5. Reduced velocity for the nonlinear system: equivalent reduced velocity

For a linear system, the reduced velocity is defined as:

$$U_r = \frac{U_\infty}{Df_{sl}}, \quad (4)$$

Here, f_{sl} represent the natural frequency of the linear system consisting of a damper (c) and linear springs with stiffnesses k and k_n .

In contrast, according to vibration mechanics, nonlinear springs have no fixed natural frequency, and hence the standard definition of reduced velocity U_r is no longer valid. Since the natural frequency of nonlinear spring depends on the vibration amplitude, the frequency cannot be calculated a priori. It can be calculated after the vibration amplitude is obtained. Once the amplitude of vibration is known, the amplitude-dependent natural frequency of the nonlinear system can be found (Kovacic and Brennan, 2011).

The motion of the cylinder in the y -direction is governed by the dimensionless equation Eq. (3). Here, Eq. (3) with the RHS set to zero is solved using a fourth-order Runge–Kutta method to derive the natural frequency ($f_s(A_{y,max}^*)$) of nonlinear spring at each amplitude. The equivalent reduced velocity can be defined as (Mackowski and Williamson, 2013):

$$U_r^{eq} = \frac{U_\infty}{Df_s(A_{y,max}^*)} = 1/f_s^*. \quad (5)$$

Further, the different reduced velocities, U_r^{eq} and U_r , are related by:

$$U_r^{eq} = \frac{U_\infty}{Df_s} = \frac{U_\infty f_{sl}}{Df_{sl}f_s} = U_r \frac{f_{sl}}{f_s}. \quad (6)$$

Here f_s represents the natural frequency of the nonlinear system consisting of the damper and springs.

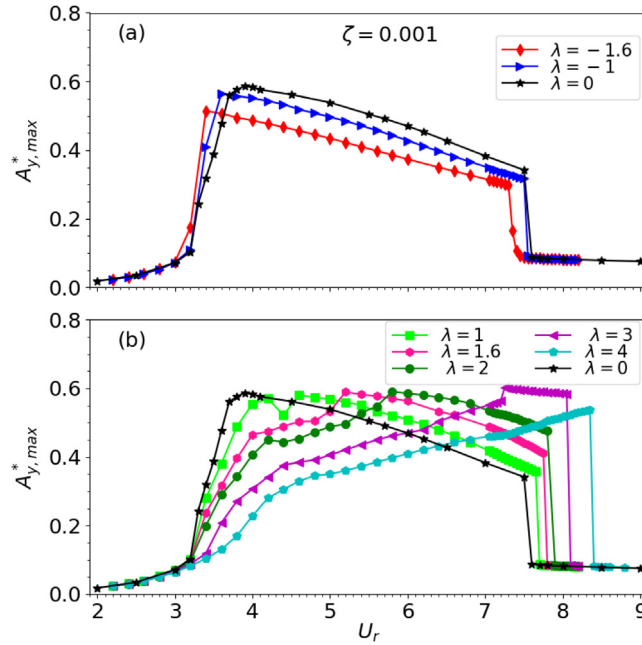


Fig. 6. The effect of nonlinear springs for $\lambda = [-1.6, 4]$ at $R = 1$ and $\zeta = 0.001$. Amplitude, A^* , versus the reduced velocity, U_r , for (a) softening; (b) hardening springs.

3. Results and discussion

The VIV of a rigid circular cylinder supported by a nonlinear viscoelastic support, which is modelled as an extended SLS model, is simulated for various values of f_n^* at $Re = 150$. There are six independent parameters in the study: mass ratio (m^*), damping ratio (ζ), spring-stiffness ratio (R), reduced velocity (U_r), Reynolds number (Re) and nonlinearity strength (λ). In this section, the effect of damping (ζ) and nonlinearity strength (λ) on the vortex-induced vibration of a circular cylinder is discussed for $m^* = 2.456$, $R = 1$. For the analysis, we have considered range of: the nonlinearity strength, $\lambda = [-1.6, 4]$; and damping ratio, $\zeta = [0.001, 10]$. For a negative value of λ , the sign of restoring force ($f_r = ky + ay^3$) is changed and the nonlinear VIV system is unstable when λ is reduced to -1.8 (Wang et al., 2019). To avoid this system instability, the lowest λ value considered is $\lambda = -1.6$.

3.1. Effect of nonlinearity strength

In this section, the effect of nonlinearity strength (λ) on the dynamic response of cylinder has been computed at five values of λ in the range $-1.6 \leq \lambda \leq 4$. First, the effect of nonlinearity on the vibration amplitude and oscillation frequency is discussed. The amplitude of displacement and peak lift coefficients are determined, noting that the frequency response helps to demarcate different VIV response branches. The branching of VIV is discussed in the subsequent subsection. Justification for classifying the different branches is further elucidated by fluid–structure dynamics and hysteresis.

3.1.1. Vibration amplitude and the frequency response

The effect of nonlinearity on the vibration amplitude of a circular cylinder is shown in Fig. 6(a) for a softening spring and Fig. 6(b) for a hardening spring. Fig. 6(a) shows that as the softening spring nonlinearity becomes stronger (i.e. λ is more negative), $A_{y,max}^*$ decreases compared to a linear spring ($\lambda = 0$). The maximum amplitude decreases from $A_{y,max}^* = 0.58$ for $\lambda = 0$ to $A_{y,max}^* = 0.51$ for $\lambda = -1.6$. The range of U_r over which large amplitude is obtained for a fixed λ decreases from $U_r = 3.2$ – 7.6 to $U_r = 3.2$ – 7.2 , corresponding to $\lambda = -1$ and $\lambda = -1.6$ respectively.

Fig. 6(b) shows the amplitude variation with reduced velocity for a hardening spring. It shows that the maximum amplitude is delayed with an increase in the nonlinearity parameter. The amplitude is maximum at $U_r = 3.9$ for $\lambda = 0$, and $U_r = 8.3$ for $\lambda = 4$. It is also observed that the range of U_r over which large amplitude is obtained for a fixed λ , increases as λ is increased. The “high-amplitude” region shifts towards the right within the range $3.4 < U_r < 7.5$ for $\lambda = 0$, to $3.4 < U_r < 8.3$ for $\lambda = 4$.

The displacement histories for $\lambda = 0$ and 4 at critical reduced velocities are presented in Figs. 7 and 8. The maximum amplitude considered in Fig. 6 is the maximum displacement of the signal. To ensure the asymptotic dynamic state was reached, the amplitude was taken over the time interval of $1050 \leq t^* \leq 1250$.

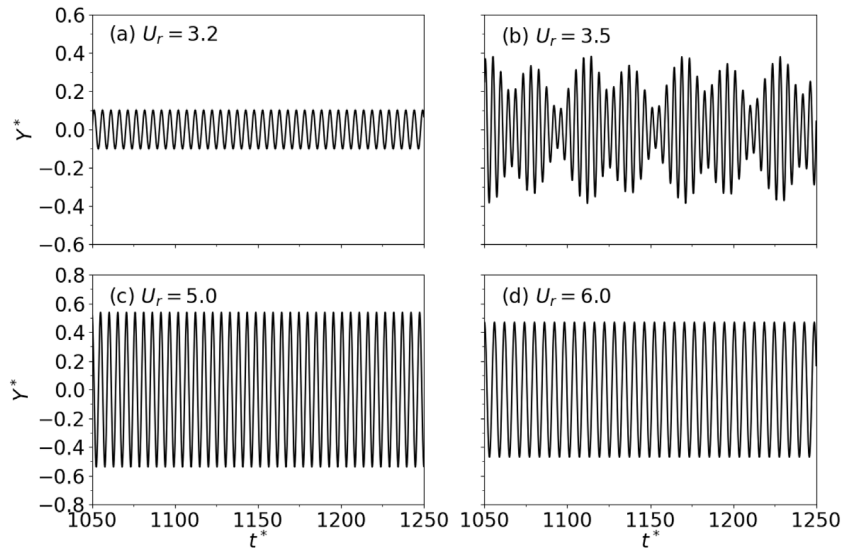


Fig. 7. The displacement history for $\lambda = 0$ at $R = 1$ and $\zeta = 0.001$ for (a) $U_r = 3.2$, (b) $U_r = 3.5$, (c) $U_r = 5.0$, (d) $U_r = 6.0$.

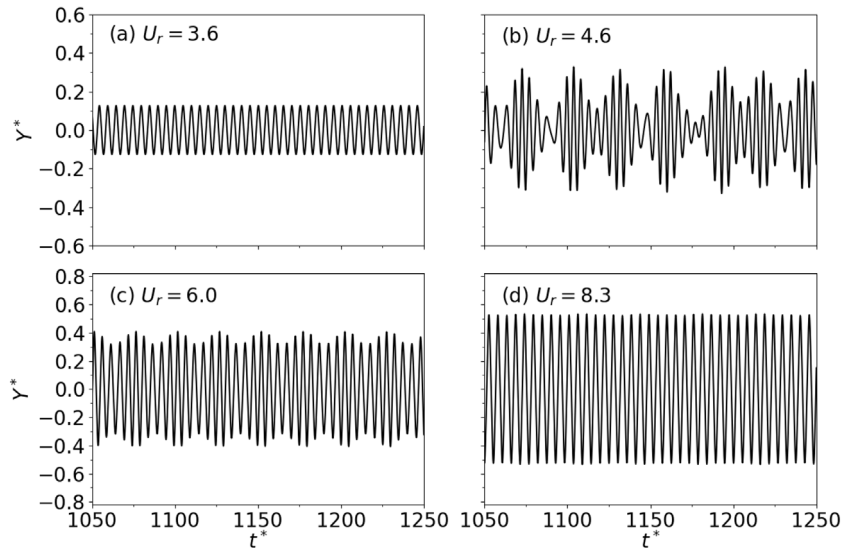


Fig. 8. The displacement history for $\lambda = 4$ at $R = 1$ and $\zeta = 0.001$ for (a) $U_r = 3.6$, (b) $U_r = 4.6$, (c) $U_r = 6.0$, (d) $U_r = 8.3$.

The variation of equivalent reduced velocity, U_r^{eq} , on VIV of a circular cylinder restrained by the extended SLS model is shown in Fig. 9. This figure helps to understand the difference between a linear viscoelastic support and nonlinear viscoelastic support. The predictions for the linear spring case ($\lambda = 0$) are included in Fig. 9 for comparison. This is consistent with the nonlinear variation between U_r^{eq} and Re , as observed by Mackowski and Williamson (2013). For a softening spring, as shown in the figure, the U_r^{eq} curves for $\lambda = -1, -1.6$, nearly collapse into a single linear curve for $\zeta = 0.1, 1, 10$. For $\zeta = 0.001$, Fig. 9(a) shows nonlinear changes of U_r^{eq} with U_r occur in the range of $U_r = 3.2-7.5$. For a hardening spring ($\lambda > 0$), as shown in Fig. 9(a), deviation from linearity starts from $U_r = 3.2$. The end of the nonlinear change is shifted towards the right as the λ is increased; ending at $U_r = 7.6$ for $\lambda = 1$ and $U_r = 8.3$ for $\lambda = 4$. The observed trend is due to variation of amplitude with U_r . Fig. 6 shows the variation of amplitude with U_r for $\zeta = 0.001, \lambda = [-1.6, 4]$. The higher the amplitude, the more the nonlinearity has an effect, and similarly for lower amplitude, the nonlinearity effect reduces. As ζ is increased, the changes due to nonlinearity decrease up to $\zeta = 1$. The trend is reversed on further increasing the damping ratio beyond $\zeta = 1$, as shown in Fig. 9. The non-monotonic trend observed is due to the structural system (SLS) considered. Please observe that the nonlinear viscoelastic system under consideration and the nondimensionalization scheme that has been followed, the current model collapses to a purely elastic system for the cases $\zeta \rightarrow 0$ and $\zeta \rightarrow \infty$ with stiffness constant k and $k + k_n$ respectively (Fig. 3).

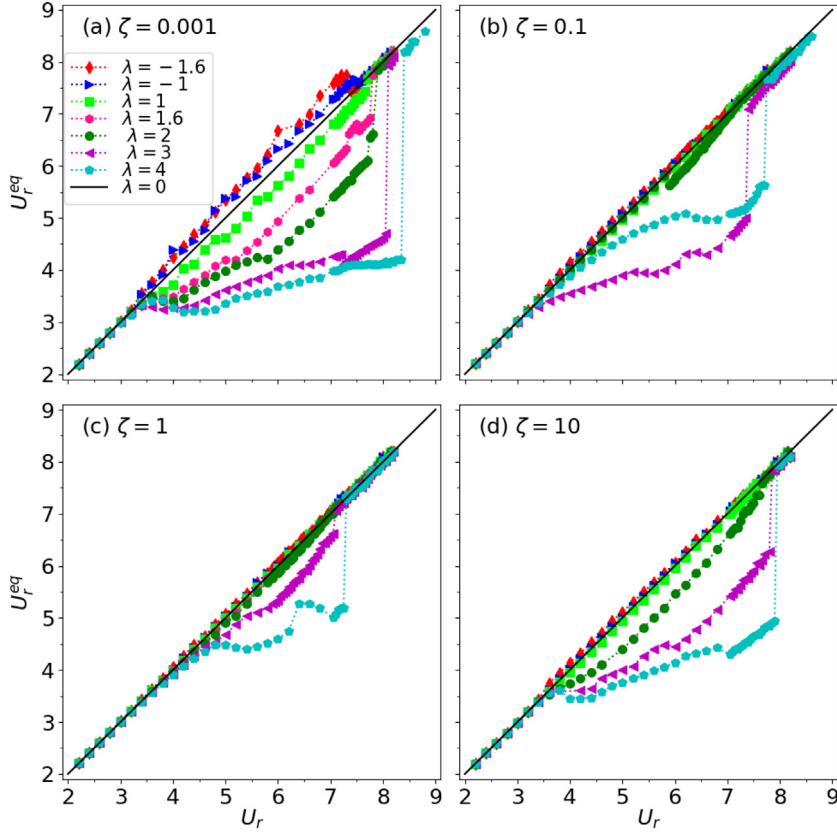


Fig. 9. Equivalent reduced velocity, U_r^{eq} , versus the linear reduced velocity, U_r , for (a) $\zeta = 0.001$, (b) $\zeta = 0.1$, (c) $\zeta = 1$, (d) $\zeta = 10$; corresponding to $R = 1$ and $\lambda = [-1.6, 4]$.

Fig. 10 show the peak lift coefficient variation with reduced velocity. The softening spring response is similar to the linear system and the peak value decreases from $C_{L,max} = 2.8$ for $\lambda = 0$ to $C_{L,max} = 1.2$ for $\lambda = -1.6$. For the hardening spring, the range of U_r over which the lift coefficient attains a near maximum (plateau) value for a fixed λ , increases as λ is increased. The peak values also increased with the introduction of nonlinearity from $C_{L,max} = 2.8$ for $\lambda = 0$ to $C_{L,max} = 3.0$ for $\lambda = 4$, although there is slight variation in peak values with nonlinearity. It shows that the effect of the hardening spring on the maximum amplitude is stronger than the softening spring.

The effect of nonlinearity on the branching behaviour of the VIV response is indicated through the frequency plot shown in **Fig. 11**. The branching behaviour for the *linear* SLS system was examined at low Re by [Mishra et al. \(2020\)](#). The upper branch in higher Re experiments is characterized by a higher oscillation amplitude than the lower branch [Williamson and Roshko \(1988\)](#). However, at low Re , the beginnings of the upper/lower branch response are not apparent through the amplitude response curve alone, but they are revealed through the lift coefficient and oscillation frequency response variations with reduced velocity. Previously it has been noted that the upper branch shows multiple frequencies in the frequency response spectrum ([Leontini et al., 2006b](#)). **Fig. 11** shows the normalized frequency, $f^* = f_y^*/f_s^*$, as a function of reduced velocity. Note that f_s^* is computed using Eq. (3) after simulations are performed, since the frequency depends on the amplitude. Here, f_y^* represents the dominant component of the vibration frequency. As illustrated in **Fig. 11**, in the initial branch, $2 < U_r < 3.2$, the vibration frequency is almost the same as the vortex-shedding frequency for a stationary cylinder for all values of λ . As demonstrated by [Mishra et al. \(2020\)](#) for a linear system (i.e. $\lambda = 0$), $3.3 \leq U_r \leq 3.9$ shows multiple frequency components, and was identified as an upper(-type) branch, followed by $4.0 \leq U_r \leq 7.5$ as a lower(-type) branch.

Figs. 11(a) and **10(a)** show that the trends obtained for $\lambda = 0$ agree with VIV under linear viscoelastic support. The strong softening results into an early departure from the lower branch to the desynchronized (**Fig. 11(a)**) region. The departure at $\lambda = -1$ from $\lambda = 0$ occurs at $U_r = 7.5$, whereas it occurs at $U_r = 7.3$ for $\lambda = -1.6$. **Fig. 11(b)** shows the frequency response for a hardening spring. With an increase of λ , the frequency response departs from the linear system frequency response. The ranges of U_r for the initial branch corresponding to $\lambda = 1, 1.6, 2$ are the same as for $\lambda = 0$, which is limited to $2 < U_r < 3.2$. For $\lambda = 1$, in the range $3.4 \leq U_r \leq 4.2$, the normalized frequency (f^*) is constant and lower than $f^* \approx 1$. In the range $3.4 \leq U_r \leq 4.2$, (see **Fig. 10(b)**) large values of the peak lift coefficient that form

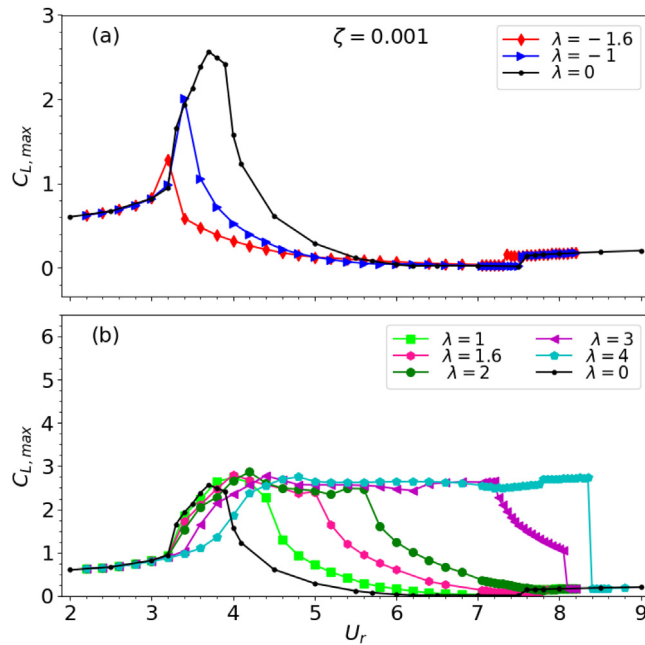


Fig. 10. Peak lift coefficients, for $R = 1$, $\zeta = 0.001$, $\lambda = [-1.6, 4]$.

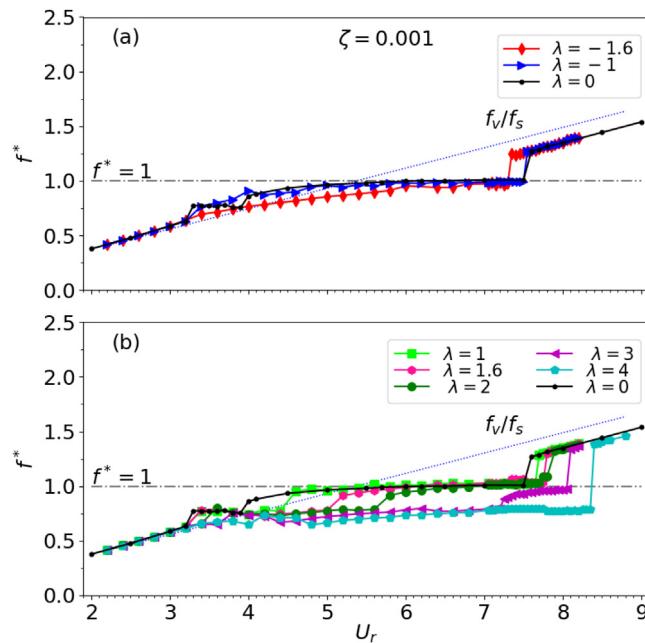


Fig. 11. The effect of nonlinear springs on frequency; Normalized frequency, f^* , versus the reduced velocity, U_r , corresponding to $R = 1$, $\zeta = 0.001$ and $\lambda = [-1.6, 4]$ for (a) softening spring, (b) hardening spring. The blue dotted line represent the vortex-shedding frequency for the stationary cylinder.

plateaus in the curves are seen, indicating the presence of the upper branch (Leontini et al., 2006b). Further, in the range $4.4 \leq U_r \leq 7.6$, $f^* \approx 1$ (see Fig. 11(b)) and the lower lift amplitude indicates the lower branch. For $U_r > 7.7$, f^* varies linearly with U_r and runs parallel with the line representing the vortex-shedding frequency for the stationary cylinder. This indicates the desynchronization region.

As illustrated in Fig. 11(b), the initial branch is extended to $2 < U_r < 3.8$ for $\lambda = 4$. Referring to Fig. 10(b), we observe the upper branch range is increased for higher values of λ . The upper branch range $3.4 \leq U_r \leq 5.8$ for $\lambda = 2$, increases to

$3.9 \leq U_r \leq 8.4$ (see Fig. 11(b)) for $\lambda = 4$. Fig. 11(b) also illustrates as the hardening of the spring increases, the departure from the lower branch to the desynchronization region is delayed. For $\lambda = 0$, the lower branch ends at $U_r = 7.5$, while for $\lambda = 4$, it ends at $U_r = 8.4$. It is interesting to note (see Fig. 11(b), Fig. 10(b)) that for $\lambda = 4$, the initial branch, upper branch and desynchronization regime are present, while the lower branch is absent.

3.1.2. Multi-frequency response, hysteresis and displacement–force phase

The nonlinearity of the system mounting leads to more complex frequency content in the amplitude and force responses than for a linear structural system. The normalized frequency ratio behaviour in the branches is shown in Fig. 12. This shows the power spectral density (PSD) of cylinder displacement (left) and the PSD of lift force signal (right) for $\lambda = 0, 1, 2, 3, 4$, shown as coloured contour plots. For all λ , in the initial branch, only one frequency component is present in the displacement and lift force signals. This corresponds to the vortex-shedding frequency of a stationary cylinder, which overlaps with the straight line representing $St = 0.19$. The wake vorticity contours shown in Fig. 14(a) show that the vortex shedding pattern is 2S and purely periodic. With a further increase in U_r , in the upper(-type) branch, multiple frequency components are present in the displacement signals, with the frequency band increasing as structural nonlinearity is increased. This emergence of multi-frequency content is clearly due to the structural nonlinearity. The PSDs of Figs. 15 and 16 show that multiple frequencies are observed in displacement (Y^*) signals in the upper branch. For the linear spring mounting, both the upper branch and lower branch are observed. For the displacement signal, the upper branch shows the presence of additional frequency content, while the lower branch shows the presence of only a single frequency. On the other hand, for the nonlinear mounting, the lower branch is absent, and increased frequency content is observed in the upper branch. It is also observed that the upper-branch U_r range is extended for the nonlinear case ($3.9 \leq U_r \leq 8.4$) as compared to the linear case ($3.3 \leq U_r \leq 3.9$). These differences can be attributed to the nonlinear structural mounting. The wake vorticity contours shown in Fig. 14(b) show the evolving wake in the upper branch ($U_r = 4.6$ for $\lambda = 4$ and $U_r = 3.5$ for $\lambda = 0$). Furthermore, in the lower branch ($f^* = 1$), the strong third harmonic for $\lambda = 0$ becomes weaker as λ is increased. At $U_r = 4.6$, Figs. 13 and 14 (and Figs. 7 and 8) show evidence of frequency modulation for the nonlinear mounting. Indeed, the instantaneous period – the time-difference between consecutive amplitude maxima (not shown) – varies by approximately 20% with displacement amplitude. This is reasonable to expect because the effective spring frequency for a nonlinear spring depends on the oscillation amplitude, which varies with time for the reduced velocity under consideration. On the other hand, for the linear spring system at $U_r = 3.5$ (see Fig. 14(a)), the amplitude modulation appears to be consistent with beating, with little variation of the instantaneous period over a beating cycle.

Figs. 15 and 16 highlight the power spectral density (PSD) for $\lambda = 0$ and $\lambda = 4$ respectively, for displacement and lift force. In the initial branch, both show strong narrow fundamental frequency content for displacement (see Figs. 15(a) and 16(a)), whereas the lift force for $\lambda = 4$ shows a weak but not negligible third harmonic. The upper branch shows a band of frequencies for both displacement and lift force. We observe the lift force for $\lambda = 4$ (Fig. 16(b)) shows a third band of frequencies approximately three times the first mode ($f_3^* \approx 3f_1^*$). As mentioned in the previous section, the upper-type branch is categorized with f^* constant but lower than $f^* = 1$. The third frequency band beyond the fundamental exists in the lift signal for $\lambda = 0$ and 4, centred at approximately three times that of the fundamental mode. The band centre for $\lambda = 4$ is lower than for $\lambda = 0$, but maintains the ratio between harmonic and fundamental frequencies of $f_3^* \approx 3f_1^*$.

Higher harmonics in the force signal have been observed in previous VIV studies with a linear structural support (e.g., Mishra et al., 2020), indicative that the forcing is not purely sinusoidal. The results presented in the current paper are consistent with these observations (see Fig. 15). These harmonics ($f_3^* = 2.89, 2.99$) are present only in the lower branch ($U_r = 5.0, 6.0$). Additional frequencies centred about the fundamental, $f_1^* = 0.77$, are also observed ($U_r = 3.5$, upper branch). Note that higher harmonics are not present in the upper branch. In contrast, for the nonlinear structural support, we observe higher harmonics in the upper branch (see Fig. 16, $U_r = 4.6, 6, 8.3$). Moreover, there are also additional frequencies, centred about the fundamental ($f_1^* = 0.71$) and third harmonic ($f_3^* = 2.25$). The increased frequency content is significant for $U_r = 4.6$, and it decreases as U_r increases.

The displacement spectra for the linear structural mounting does not show any significant higher harmonic content. We do see a few additional frequencies centred about the fundamental ($f_1^* = 0.77$) in the upper branch, but these are absent in the lower branch. The displacement spectra for the structure with a nonlinear support also does not show any appreciable higher harmonics but we do see additional frequency content centred around the fundamental in the upper branch. This additional frequency content is significant for $U_r = 4.6$ but reduces as U_r increases. Hence, it is clear that the presence of the structural nonlinearity causes an appreciable change in both the displacement and force spectra. However, beyond this, perhaps the most significant difference between the response for the linear and nonlinear structure mounting is the absence of a lower branch in the latter case.

The cylinder response may exhibit hysteresis due to a delay in mode-switching during a transition. Hysteresis may be caused by the nonlinearity of the system, flow, or structural components. As shown in Fig. 17, the present simulation results display hysteretic behaviour. Brika and Laneville (1993) have observed that the cylinder response is sensitive to changing the reduced velocity in small increments, ΔU_r . As the reduced velocity is defined as the inverse of the oscillator natural frequency, computations of hysteresis have been carried out with decrements of the structural natural frequency, Δf_n^* . For the increasing-velocity curve, the reduced velocity is increased from $U_r = 2$ in small increments with the initial condition at each U_r being the saturated response at the previous increment. The reduced velocity is increased by

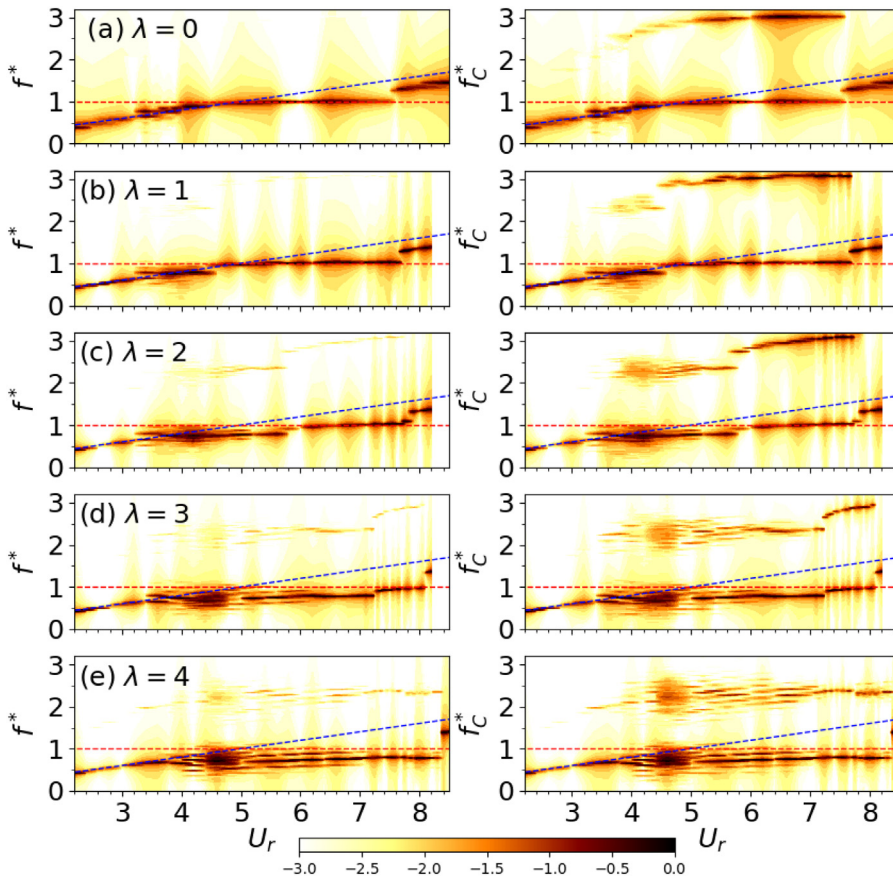


Fig. 12. Contour of the power spectral density of displacement(left) and lift force(right) plotted against the normalized frequency and reduced velocity U_r for $\zeta = 0.001$. The spectral power is normalized by the respective maximum value at each U_r . A \log_{10} scale is used to better highlight the variation from 0 (black) to -3 (white).

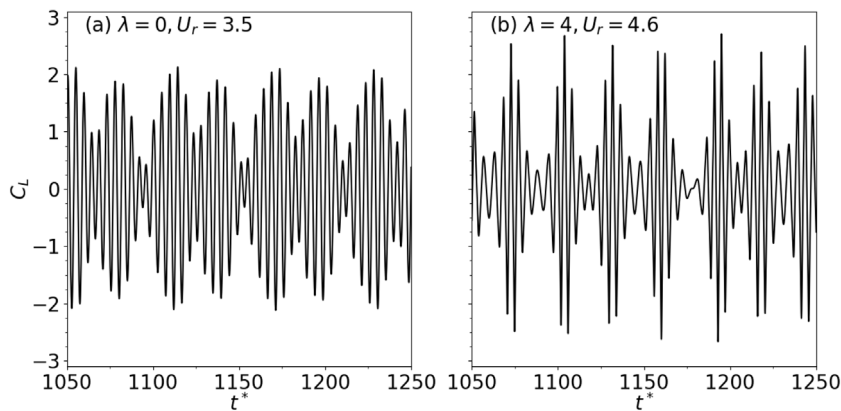


Fig. 13. Time-dependent lift coefficients (C_L) plot for (a) $\lambda = 0, U_r = 3.5$; (b) $\lambda = 4, U_r = 4.6$.

decreasing the non-dimensional linear structural natural frequency, f_n^* , with the decrement size taken is $\Delta f_n^* = 0.001$. For the decreasing velocity-curve, the reduced velocity is decreased from $U_r = 12$ by increasing f_n^* , with the initial condition again corresponding to the fully saturated state for the next level of U_r . A very small hysteretic loop is observed at the onset of the upper-type branch in the range of $3.2 \leq U_r \leq 3.3$. Hysteresis for the transition between the upper branch and desynchronization regime is shown in Fig. 17. This occurs over a much wider reduced velocity range for the nonlinear case ($8 \leq U_r \leq 12$) than in the linear case ($7.35 \leq U_r \leq 8.58$). Since both the structural and fluid components are

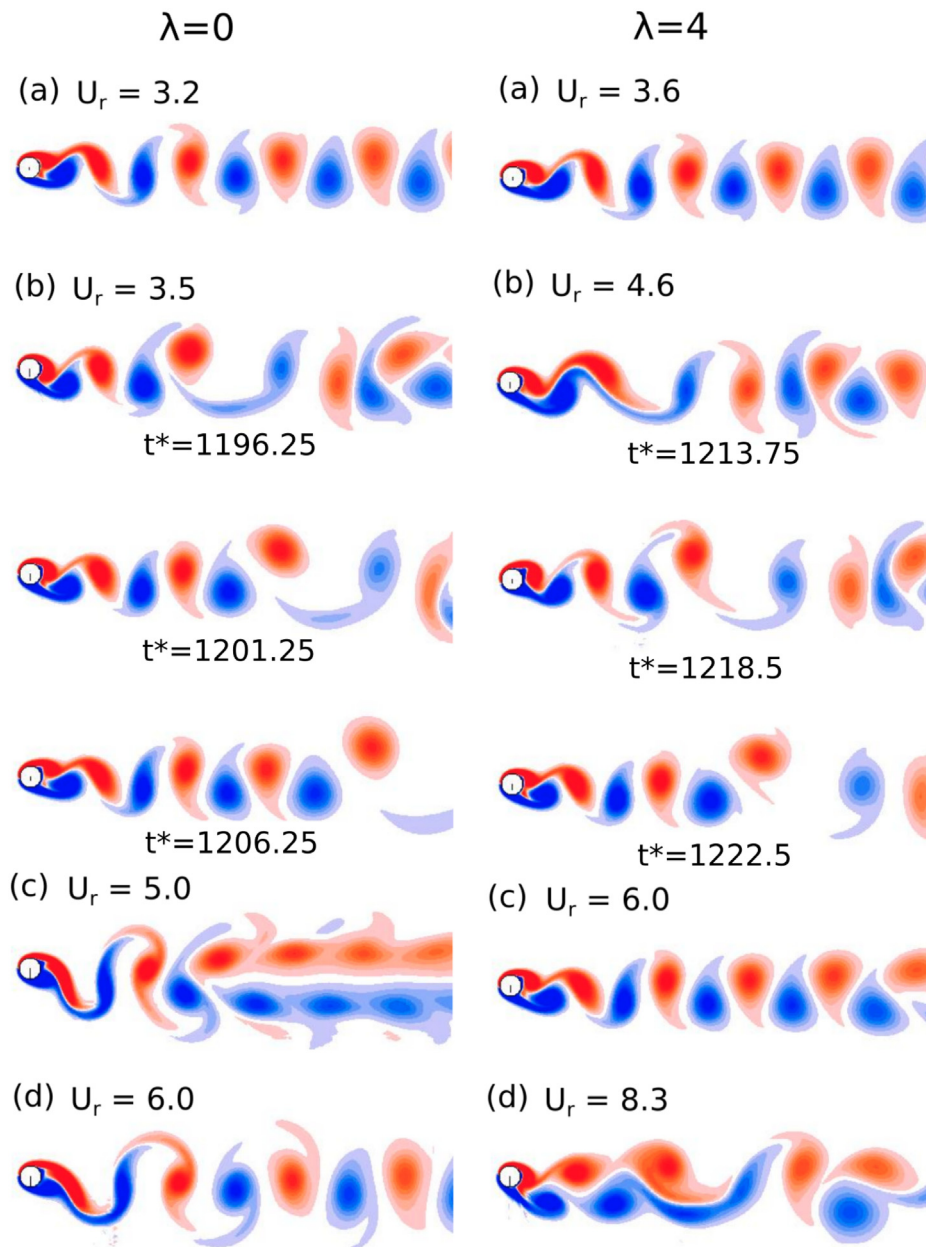


Fig. 14. Vorticity contours (scale -2 to 2) for $\zeta = 0.001$ at U_r representing response branches. For $\lambda = 0$ (a) $U_r = 3.2$ (Initial branch), (b) $U_r = 3.5$ (Upper-type branch), wake evolution over time, (c) $U_r = 5.0$ (Lower branch), (d) $U_r = 6.0$ (Lower branch). For $\lambda = 4$ (a) $U_r = 3.6$ (Initial branch), (b) $U_r = 4.6$ (Upper-type branch), wake evolution over time, (c) $U_r = 6.0$ (Upper-type branch), (d) $U_r = 8.3$ (Upper-type branch).

nonlinear, hysteresis originates from both and the loop is wider than the corresponding linear VIV system where only the fluid component contributes to the nonlinearity.

The phase difference between fluid force and cylinder displacement is an important quantity to describe the nature of the vortex-induced vibration. Fig. 18 shows the effect of nonlinearity on the total phase difference, ϕ_{tot} , and the phase difference between vortex force (lift component) and the displacement, ϕ_{vort} . The total phase difference, ϕ_{tot} , is given from the mean value of the instantaneous total phase difference between the lift and displacement, obtained using a Hilbert transform (Khalak and Williamson, 1999; Mishra et al., 2020), whereas for ϕ_{vort} , the vortex force (Williamson and Govardhan, 2004) is considered. The jump in ϕ_{tot} occurs between the upper and lower branches, whereas there is a jump in ϕ_{vort} at the initial to upper branch transition.

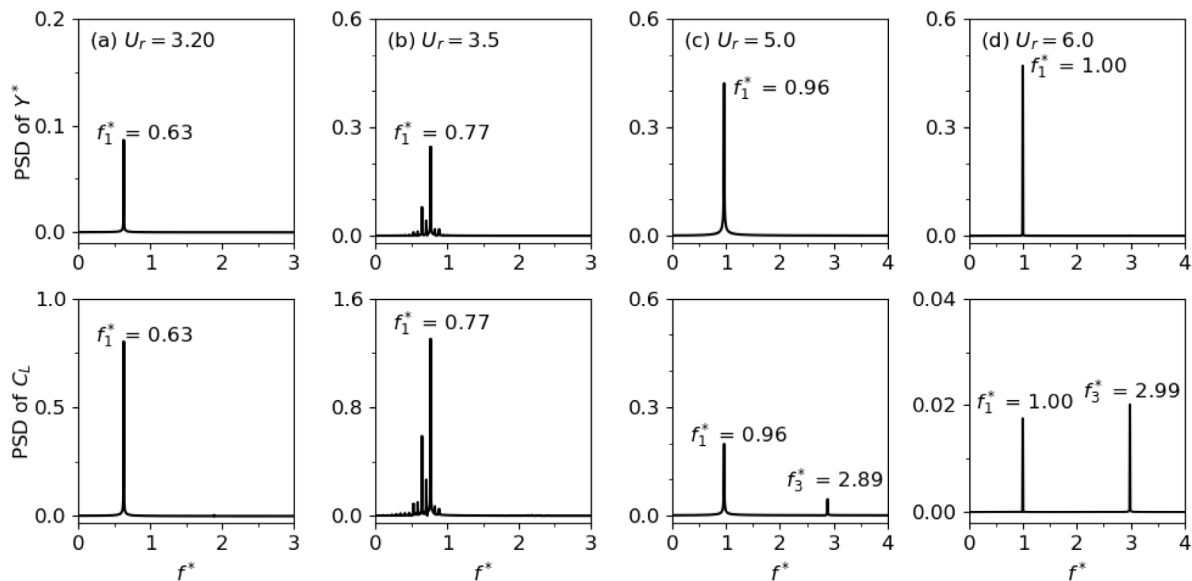


Fig. 15. Power spectral density (PSD) for $R = 1$, $\zeta = 0.001$ and $\lambda = 0$, indicating the modes of frequencies of displacement and lift force representing the response branches, for (a) $U_r = 3.2$ (Initial branch), (b) $U_r = 3.5$ (Upper-type branch), (c) $U_r = 5.0$ (Lower branch), (d) $U_r = 6.0$ (Lower branch).

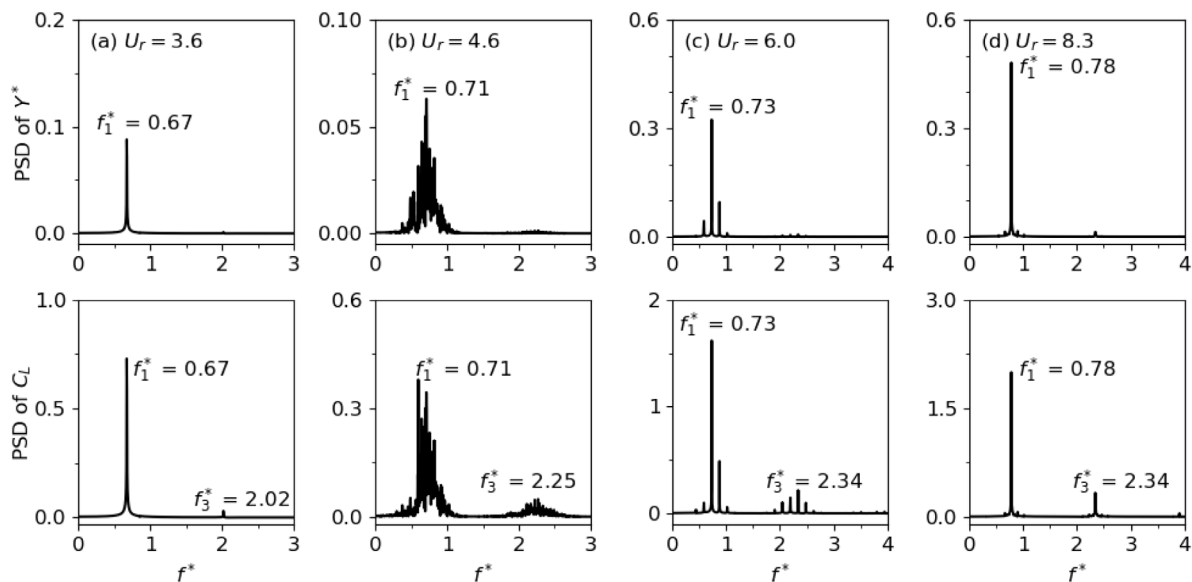


Fig. 16. Power spectral density (PSD) for $R = 1$, $\zeta = 0.001$ and $\lambda = 4$, indicating the modes of frequencies of displacement and lift force representing the response branches, for (a) $U_r = 3.6$ (Initial branch), (b) $U_r = 4.6$ (Upper-type branch), (c) $U_r = 6.0$ (Upper-type branch), (d) $U_r = 8.3$ (Upper-type branch).

Fig. 18(a) reveals that as the softening spring nonlinearity increases, the change in phase difference from $\phi_{tot} = 0^\circ$ to $\phi_{tot} = 180^\circ$, corresponding to the transition from upper to lower branch, occurs earlier, from $U_r = 5$ for $\lambda = -1$ to $U_r = 3.1$ for $\lambda = -1.6$. Fig. 18(c) shows the jump in $\phi_{vort} = 0^\circ$ to 180° , corresponding to the transition from initial to upper branch, advances from $U_r = 3.4$ for $\lambda = -1$ to $U_r = 3.2$ for $\lambda = -1.6$. Fig. 18(b) and (d) show the effect of the hardening spring nonlinearity on the phase difference. Fig. 18(b) reveals as the nonlinearity grows from $\lambda = 1$ to $\lambda = 4$, the change in ϕ_{tot} , corresponding to the transition from upper to lower branch, is delayed from $U_r = 6.2$ for $\lambda = 1$ to $U_r = 8.4$ for $\lambda = 4$. The jump in ϕ_{vort} is also delayed from $U_r = 4.4$ for $\lambda = 1$ to $U_r = 8.4$ for $\lambda = 4$, corresponding to transition from the initial to the upper branch.

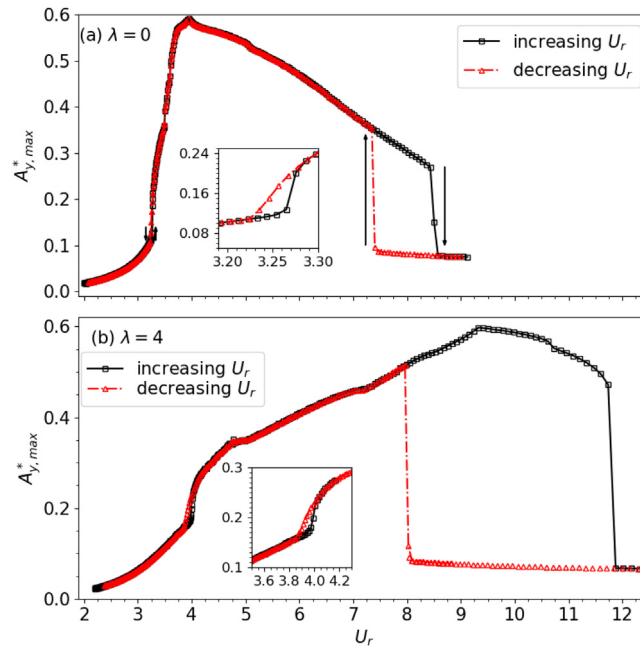


Fig. 17. Amplitude response of the cylinder. Variation of amplitude versus reduced velocity for $\zeta = 0.001$, for (a) $\lambda = 0$, (b) $\lambda = 4$, $R = 1$, showing the effect of slowly increasing and decreasing the reduced velocity.

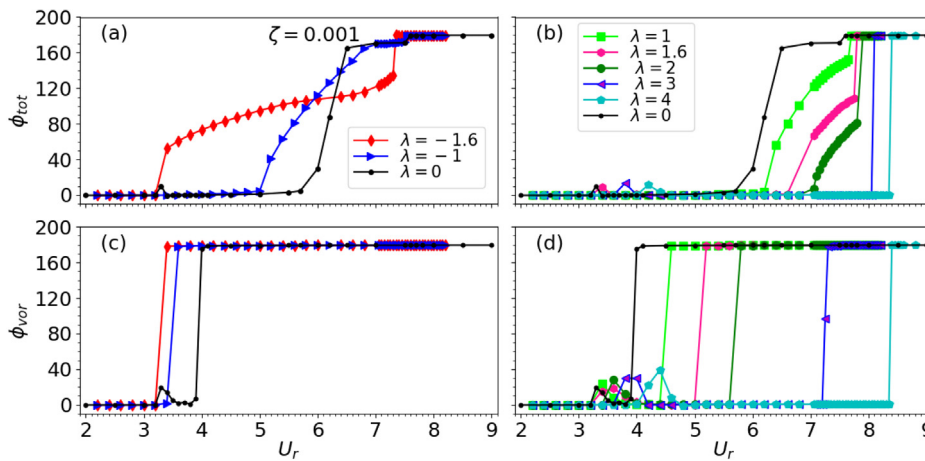


Fig. 18. Phase difference between displacement and lift force, ϕ_{tot} , for $\zeta = 0.001$, for (a) $\lambda = -1.6, -1, 0$ and (b) $\lambda = 1, 1.6, 2, 3, 4$. Phase difference between displacement and vortex force, ϕ_{vor} , for (c) $\lambda = -1.6, -1, 0$ and (d) $\lambda = 1, 1.6, 2, 3, 4$. All variables are plotted against reduced velocity for parameters $\zeta = 0.001$ and $R = 1$.

3.2. Effect of damping ratio

This section presents the effects of damping on VIV of the cylinder, supported by an extended SLS system. The dynamic response of cylinder has been calculated at six values of damping ratio for $0.001 \leq \zeta \leq 10$, for the two extreme nonlinear cases previously considered: $\lambda = -1.6$ and 4 .

3.2.1. Vibration amplitude response

Fig. 19 shows the amplitude versus reduced velocity for the softening spring. Fig. 19(a) shows the amplitude and peak lift coefficient response is similar to the linear VIV system as observed by Mishra et al. (2020). For the softening spring, the characteristic are similar to the linear system. Mishra et al. (2020) explained the effect of damping ratio on amplitude and lock-in for the linear SLS system. The vibration amplitude Fig. 19(a) decreases with an increase in the damping ratio until reaching $\zeta = 1$. On further increasing the damping, the amplitude increases. Fig. 19(c) shows the lock-in region is

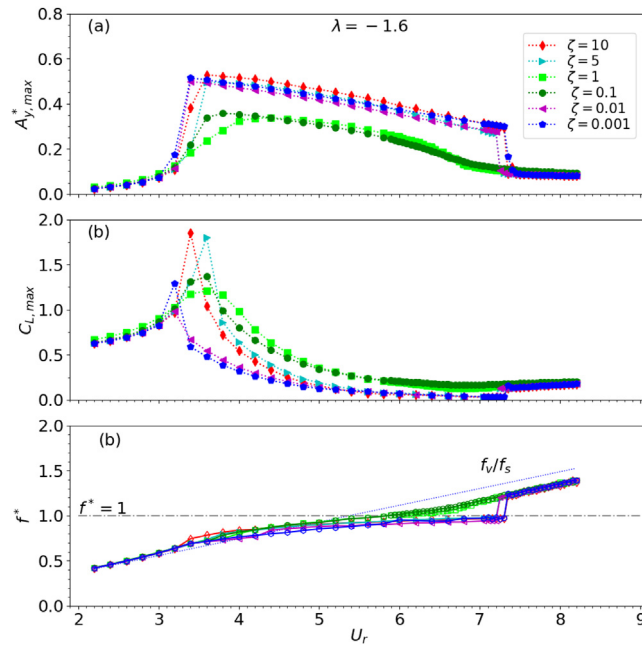


Fig. 19. The effect of damping on softening (nonlinear) springs: (a) amplitude, (b) peak lift coefficient, (c) normalized frequency. All plots are w.r.t. linear reduced velocity, U_r , for $R = 1$, $\zeta = [0.01, 10]$ and $\lambda = -1.6$. The blue dotted line in (c) represents the vortex-shedding frequency for the stationary cylinder. (For interpretation of the references to colour in this figure legend, the reader is referred to the web version of this article.)

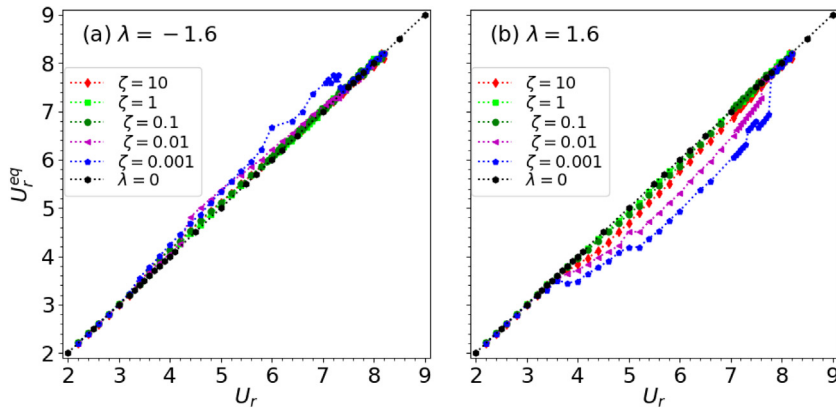


Fig. 20. The effect of damping nonlinear springs. Equivalent reduced velocity, U_r^{eq} , versus the linear reduced velocity, U_r , for $R = 1$ and $\zeta = [0.01, 10]$: (a) $\lambda = -1$, (b) $\lambda = -1.6$.

non-monotonic with damping ratio. The departure for desynchronization is shifted towards the left from $\zeta = 0.001$ to $\zeta = 1$. The end of the initial branch is shifted towards the right for $\zeta = 0.001$ to $\zeta = 1$. Beyond $\zeta = 1$, desynchronization is shifted towards the right, and the end of the initial branch is shifted towards the right, for $\zeta = 1$ to $\zeta = 10$.

In Fig. 20(a), the equivalent reduced velocity, U_r^{eq} is plotted against the reduced velocity, U_r , for the softening spring. Fig. 20(a) clearly shows the effect of damping is not prominent at $R = 1$. As observed that for different values of ζ , the effective nonlinearity is very close to the linear ($\lambda = 0$) curve. Also the curve lies above that for a linear spring for a softening spring (see Fig. 20(a)), and below that for a linear spring for a hardening spring (see Fig. 20(b)). The contrast in behaviour of the softening and hardening systems is shown in Fig. 20. This shows the stronger effect of hardening on the VIV system than softening for the same nonlinearity parameter magnitude. The curve for a nonlinear spring has also been reported in the experimental study of Mackowski and Williamson (2013); however, they considered U_r^{eq} versus Re instead of U_r^{eq} versus U_r . They presented results that for a linear spring U_r^{eq} and Re are proportional, given the experimental setup where the flow velocity changes both proportionally. However, for a nonlinear spring system studied here, U_r^{eq} can vary independently of Re .

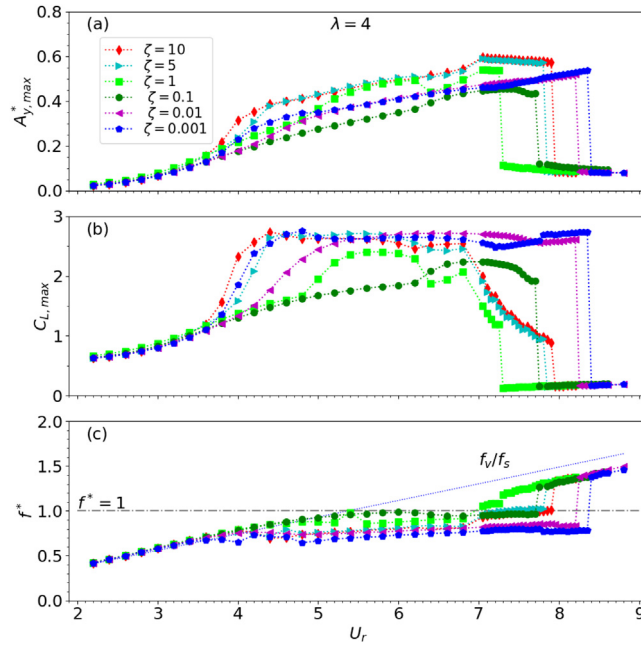


Fig. 21. (a) Amplitude of displacement $A_{y,max}^*$; (b) peak lift coefficient $C_{L,max}$; (c) normalized frequency f^* . All are plotted versus reduced velocity, U_r , for $\lambda = 4$, $\zeta = [0.001, 10]$ and $R = 1$. The blue dotted line in (c) represents the vortex-shedding frequency for the stationary cylinder. (For interpretation of the references to colour in this figure legend, the reader is referred to the web version of this article.)

Fig. 21 shows the amplitude of vibration, peak lift coefficient and frequency response with U_r for $\lambda = 4$. The cylinder displacement, $A_{y,max}^*$ increases continuously up to a maximum value and subsequently suddenly drops with increasing U_r . It depicts the location of the peak amplitude non-monotonically varies with ζ . Fig. 21(a) shows the peak amplitude for $\zeta = 0.001$ occurs at $U_r = 8.4$, decreases to $U_r = 7.2$ for $\zeta = 1$, and further increases to $U_r = 8$ for $\zeta = 10$. This is in contrast to $\lambda = -1.6$ (Fig. 19(a)), where the peak amplitude decreases with U_r in the synchronization region. Fig. 21(b) shows the plateaued peak lift coefficient, $C_{L,max}$, and the range of U_r corresponding to the plateau varies non-monotonically with ζ . The peak lift corresponding to the plateau is limited to $4.6 < U_r < 8.4$ for $\zeta = 0.001$, decreases to $5.3 < U_r < 6.2$ for $\zeta = 1$, and then the limit further increases to $4.4 < U_r < 6.8$ for $\zeta = 10$. In contrast to a softening spring, with $\lambda = -1.6$, (Fig. 19(b)), the peak lift decreases with U_r in the synchronization region.

Fig. 21(c) shows the normalized frequency ratio of the vibration frequency to the natural frequency of the nonlinear damped system, f_y^* . The range of U_r showing a constant value of f_y^* is known as the lock-in region. The figure depicts, for the plateau range of f_y^* , although constant, the value is less than 1. For $\zeta = 0.001$, $f_y^* \approx 0.7$ for $4.6 < U_r < 8.4$, the range where the peak lift is approximately constant. For $\zeta = 0.1$, $f_y^* \approx 1$ in $5.2 < U_r < 7.7$, and the peak lift is continuously increasing. For $\zeta = 10$, $f_y^* \approx 0.8$ in $4.0 < U_r < 6.8$ where the peak lift is constant. Further $f_y^* \approx 1$ for $7.0 < U_r < 7.9$ where the lift coefficient is decreasing. The results show that the maximum amplitude, peak lift coefficient and region of constant frequency are non-monotonic with damping. For $\zeta = 0.001$, $A_{y,max}^* = 0.53$, $C_{L,max} = 2.75$, $f_y^* \approx 0.7$. For $\zeta = 0.1$, the amplitude and peak lift decrease to $A_{y,max}^* = 0.43$ and $C_{L,max} = 2.2$, and the normalized frequency increases to $f_y^* = 1$. On further increases of ζ , the amplitude and peak lift increase; these values for $\zeta = 10$ are $A_{y,max}^* = 0.59$, $C_{L,max} = 2.55$ and the normalized frequency decreases to $f_y^* = 0.8$.

For the nonlinear viscoelastic support, the VIV results can be explained by understanding the relationship between the reduced velocity, U_r , and the equivalent reduced velocity, U_r^{eq} . The plot of Fig. 9 shows the equivalent reduced velocity, U_r^{eq} , versus the reduced velocity, U_r , for different damping ratios for the hardening spring. For a linear spring, U_r^{eq} and U_r are the same and hence the plot is linear; however, for a system with nonlinear springs the quantities are different and vary independently within a range. Of course, this is attributed to the ability of a system with nonlinear spring to change its natural frequency with amplitude. Fig. 9 shows the effective nonlinearity is non-monotonically varying with ζ . Fig. 9(a) shows that at a very low value of damping ratio ($\zeta = 0.001$), the effective nonlinearity is high as the curve departs from the linear curve ($\lambda = 0$). As the damping is increased (Fig. 9(b,c)), the effective nonlinearity decreases, since the curve then moves closer to the $\lambda = 0$ curve. On further increases of damping ratio beyond $\zeta = 1$, at $\zeta = 10$ (Fig. 9(d)), the effective nonlinearity increases as the curve is again moved away from $\lambda = 0$. We also observe the range of nonlinearity is non-monotonic with ζ . It shows that the nonlinearity range is $3.4 < U_r < 8.4$ for $\zeta = 0.001$, and the range shortens to $3.9 < U_r < 7.3$ for $\zeta = 1$. On further increasing ζ , the range further widens to $3.5 < U_r < 8$ for $\zeta = 10$. The effect of damping is more prominent for higher values of λ , but at low values of λ the curve is very near to linear. Fig. 9 clearly

shows for different value of ζ the effective nonlinearity is very close to that of the linear ($\lambda = 0$) curve. The observed non-monotonic behaviour with respect to ζ is due to the structural system considered. As discussed, it can be observed that if $\zeta \rightarrow \infty$, the extended SLS model collapses to a spring-mass system with two parallel springs with one of them being nonlinear (see Fig. 3(b)). Again for $\zeta = 0$, the extended SLS model collapses to a spring-mass system with a single nonlinear spring (see Fig. 3(a)).

3.2.2. Branching behaviour and lock-in regimes as a function of damping

The effect of damping (ζ) on synchronization of the vibration response of a cylinder supported by the nonlinear spring combination is shown in Fig. 21. In the initial branch, $2.2 \leq U_r \leq 4.2$, for $\zeta = 0.001$ the vibration response is influenced by the vortex shedding frequency for a stationary cylinder. In the lower branch, $4.4 \leq U_r \leq 8.4$, the vibration frequency locks to the natural frequency of the system (see Fig. 21(c)) and the amplitude increases continuously (see Fig. 21(a)). The amplitude jumps down to small values for $U_r > 8.5$ – the desynchronization region.

The higher amplitude response of the system takes place in the lock-in or resonance range. To explain the lock-in regimes over different ζ and U_r , and to delimit the different branches in VIV, a normalized frequency plot is used. As previously indicated, Fig. 21(c) represents the normalized frequency: the ratio of the vibration frequency to the natural frequency of the nonlinear system (f_s). The vibration frequency (f_y) corresponds to the peak of the power spectrum of the displacement. Note that the natural frequency of the nonlinear system is computed using Eq. (3) after simulations are performed since the frequency depends on the initial conditions. Fig. 21 shows the lock-in regime for the hardening spring for a low value of damping ratio, $\zeta = 0.001$, where the vibration frequency is lower than the natural frequency of the system. As the damping ratio increases, the vortex shedding frequency approaches to the natural frequency up to $\zeta = 0.1$. On further increases of ζ , the vortex shedding frequency again moves away from the natural frequency. The range of lock-in is also non-monotonic with ζ . For $\zeta = 0.001$, it lies in the range $3.8 \leq U_r \leq 8.3$, shifting to $5.4 \leq U_r \leq 7.8$ for $\zeta = 0.1$. The range again increases to $3.8 \leq U_r \leq 7.9$ for $\zeta = 10$. For $\zeta = 0.001$, Fig. 21(c) shows for range $2 \leq U_r \leq 3.8$, f^* coincides with the vortex shedding of a stationary cylinder, corresponds to the initial branch. For the range $3.9 \leq U_r \leq 8.3$, f^* is constantly lower than $f^* \approx 1$, and the peak lift coefficient has a higher value, which corresponds to the upper branch. For $U_r \geq 8.4$, the curve of f^* is parallel to the vortex shedding frequency of a stationary cylinder, indicating the desynchronization region. The normalized frequency plot and peak lift force variation clearly indicate the missing lower branch for $\zeta = 0.001$. For $\zeta = 0.1$, there is an initial branch, $2 \leq U_r \leq 5.4$, lower branch, $5.5 \leq U_r \leq 7.8$ and desynchronization for $U_r > 7.8$, but the upper branch is absent. Further increasing the damping to $\zeta = 10$, we observe the initial branch in the range $2 \leq U_r \leq 3.8$, the upper branch between $3.9 \leq U_r \leq 6.8$, the lower branch in $6.8 \leq U_r \leq 7.9$, and desynchronization for $U_r \geq 8.0$. Once again, this non-monotonic characteristic for the existence of the standard response branches is due to the structural system (SLS) considered.

Fig. 22 depicts the phase difference between the lift force and the displacement against U_r for different values of ζ at $\lambda = 4$. Fig. 22 shows the jump in the phase difference changes from $\phi_{tot} \approx 0^\circ$ to $\phi_{tot} \approx 180^\circ$. There is non-monotonic variation in the reduced velocity at which the jump occurs with ζ . For $\zeta = 0.001$, the jump occur at $U_r = 8.4$, indicating the switch from the upper to the desynchronization branches. The jump decreases to $U_r = 7.3$ for $\zeta = 1$, marking the change from the lower to desynchronization branches. On further increasing ζ beyond $\zeta = 1$, the jump increases to $U_r = 8.0$ for $\zeta = 10$. This change in the phase difference at the transition between the lower and desynchronization branches is in contrast to the change of phase difference at the upper to lower transition observed by Khalak and Williamson (1999). This difference in phasing is presumably due to the low Reynolds number and high nonlinearity investigated. The non-monotonic variation of the jump with ζ is not visible for ϕ_{vor} . The jump occurs at $U_r = 8.4$ for $\zeta = 0.001$, indicating transition from the upper branch to desynchronization. The jump in ϕ_{vor} decreases to $U_r = 6.8$ for $\zeta = 1, 5, 10$, at the switch from the upper branch to the lower branch. This jump in the vortex phase was observed in high Reynolds number experiments of Govardhan and Williamson (2000) at the initial to upper branch transition.

The vortex shedding patterns spanning the jump in phase difference are shown in Fig. 23. In all cases, a 2S vortex shedding mode is observed. At the jump of ϕ_{tot} , the shedding pattern changes from a double-row configuration to a single-row configuration (Leontini et al., 2006b). For $\zeta = 0.001, 1$, and 10 , the jumps occur at $U_r = 8.4, 7.3$ and 8.0 respectively. We also observed at the jump of ϕ_{vor} , a double-row 2S configuration, but with a slight variation in the positioning of vortices in the wake.

4. Conclusions

The effects of a nonlinear viscoelastic support on the response of cross-flow vortex-induced vibration of a circular cylinder have been investigated numerically, for the mass ratio of $m^* = 2.546$ at $Re = 150$. The spring-damper system used to provide viscoelastic support is similar to the Standard Linear Solid (SLS) model and is referred to as the extended SLS model. It consists of two springs and one damper, where the two springs are in parallel, and the damper is in series with one of the springs. The spring in series with damper is linear, and that parallel to the damper is nonlinear. The nonlinear structural system is governed by the following three parameters: (a) the ratio of spring constants (R), (b) the damping ratio (ζ), and (c) the nonlinearity strength (λ). The focus of the present study is to examine the response of the cylinder to VIV by changing ζ and λ . The dimensionless nonlinearity strength (λ) is varied from -1.6 to 4 . We observe that the peak amplitude decreases in comparison to the linear spring, as spring softening ($\lambda < 0$) is increased. In contrast,

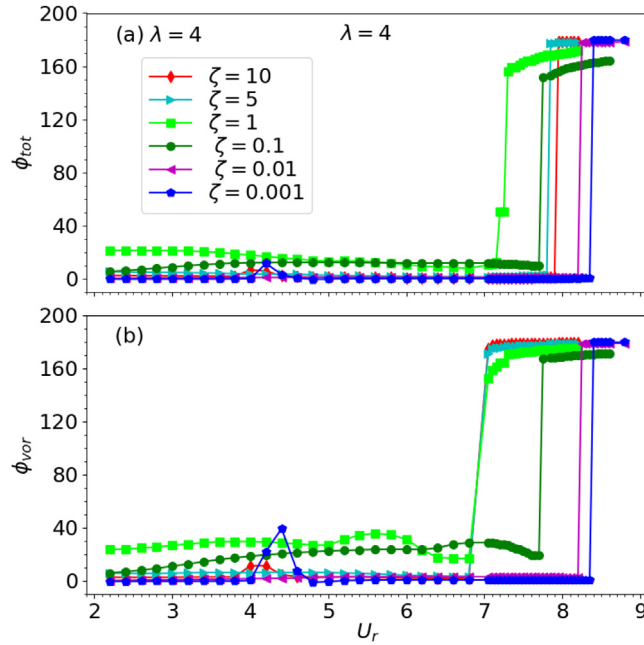


Fig. 22. (a) Phase difference between displacement and lift force; (b) Phase difference between displacement and vortex force; All variables are plotted against reduced velocity for $\lambda = 4$, $\zeta = [0.001, 10]$, $R = 1$.

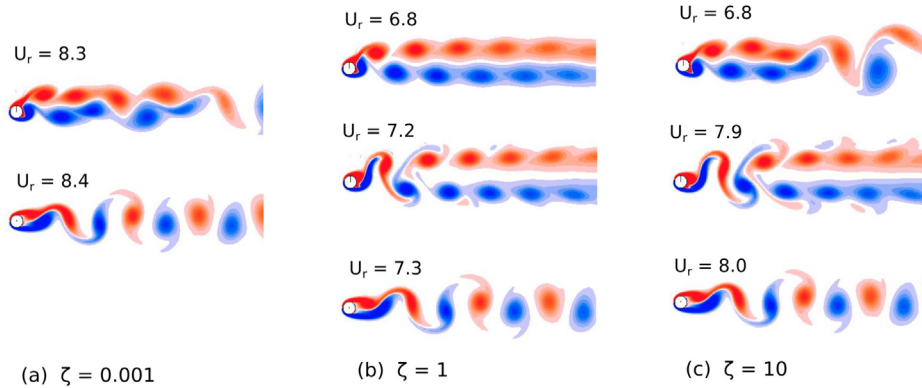


Fig. 23. The wake evolution for $\lambda = 4$, representative of the variation in the wake observed for transformation of branch. (a) $\zeta = 0.001$; (b) $\zeta = 1$; (c) $\zeta = 10$.

the peak amplitude for the hardening spring ($\lambda > 0$) increases with λ . The equivalent reduced velocity is affected by damping, showing a non-monotonic variation with ζ . We also observed that for a high value of $\lambda \geq 3$, the peak lift force coefficient is constant over a range of reduced velocity for both very low and high values of damping.

The softening spring ($\lambda < 0$) shows response regimes consisting of initial, upper, lower, and desynchronized branches. The behaviour of the system with $\lambda = -1$ is similar to a linear system. For a softening spring with $\lambda = -1.6$, the lock-in region becomes narrower and there is an early departure to the desynchronized region. The hardening spring with weaker hardening ($\lambda \in [1, 3]$) shows the initial, upper, lower, and desynchronized branches, whereas for $\lambda = 4$, the lower branch is absent. As the nonlinearity parameter increases, the lock-in region becomes wider and a late departure to the desynchronized region occurs. This trend is observed for a very high value of the nonlinear parameter. The response is the same for very low and high values of the damping ratio ($\zeta = 0.001, 10$). For a system with a high nonlinearity parameter at ($\lambda = 4$) at $\zeta = 0.001, 10$, the lower branch is missing. This is confirmed by the consideration of the peak lift coefficient, the existence of multiple frequencies, and the normalized frequency response.

The vibration amplitude and lift force also show a non-monotonic variation with increasing damping for systems with hardening and softening springs. A similar trend is observed for the total phase difference, where the jump of ϕ_{tot} from

0° to 180° is delayed for $\zeta = 0.001$. As damping is increased, an early arrival of the jump occurs up to $\zeta = 1$. On further increasing ζ beyond $\zeta > 1$, a delayed jump is observed. The vortex phase difference also shows a jump of 0° to 180°. The U_r for the jump is decreased with increases in damping, whereas the jump does not change for $\zeta \geq 1$. This study shows VIV is more influenced by a hardening spring than a softening spring. This study also shows a non-monotonic variation of amplitude with the damping ratio.

A system with a hardening stiffness element has a varying natural frequency that depends upon its excitation amplitude. This results in a potential way to widen the lock-on range as evident from the observed plateau value of the peak lift coefficient. This could be a useful method to extract energy for a wider range of reduced velocity in energy harvesting applications. In the present study, the structural nonlinearity is due to the nonlinearity of the spring. The influence of nonlinear damping will be explored in a future study.

CRediT authorship contribution statement

Rahul Mishra: Conceptualization, Software, Investigation, Writing - original draft. **Rajneesh Bhardwaj:** Discussion, Writing - review & editing. **Salil S. Kulkarni:** Discussion, Writing - review & editing. **Mark C. Thompson:** Software, Discussion, Writing - review & editing.

Declaration of competing interest

The authors declare that they have no known competing financial interests or personal relationships that could have appeared to influence the work reported in this paper.

Appendix. Equation of motion for a nonlinear SLS supported system

Considering the spring in series with the dashpot is linear whereas that parallel to the dashpot is nonlinear, as shown in Fig. 1, the force versus displacement relation is given by

$$f_1 = kx + ax^3, \quad (\text{A.1})$$

$$f_2 = k_n x_1. \quad (\text{A.2})$$

In parallel, forces are added while displacement remains the same, whereas in series, forces remain the same while displacements are added. The above arguments together with the structure force ($F = F_{struct}$) is given by

$$F_{struct} + \frac{c}{k_n} \frac{dF_{struct}}{dt} = kx + ax^3 + \frac{c}{k_n} (k + 3ax^2 + k_n) \frac{dx}{dt} \quad (\text{A.3})$$

If we combine the structure equation with the dynamic equation:

$$m \frac{d^2x}{dt^2} = F_{ext} - F_{struct}, \quad (\text{A.4})$$

we get

$$\frac{c}{k_n} m \frac{d^3x}{dt^3} + m \frac{d^2x}{dt^2} = \frac{c}{k_n} \frac{dF_{ext}}{dt} + F_{ext} - \left(\frac{c}{k_n} \frac{dF_{struct}}{dt} + F_{struct} \right). \quad (\text{A.5})$$

Now substituting the expression for $\left(\frac{c}{k_n} \frac{dF_{struct}}{dt} + F_{struct} \right)$ from Eq. (A.3) in Eq. (A.5), gives

$$\frac{mc}{k_n} \frac{d^3x}{dt^3} + m \frac{d^2x}{dt^2} + c \left(1 + \frac{a}{k_n} 3x^2 + \frac{k}{k_n} \right) \frac{dx}{dt} + kx + ax^3 = F_{ext} + \frac{c}{k_n} \frac{dF_{ext}}{dt}. \quad (\text{A.6})$$

Eq. (A.6) is the third-order differential equation governing the motion of cylinder under the nonlinear spring support. Further using $R = \frac{k_n}{k}$, $\zeta = \frac{c}{2\sqrt{km}}$ and $\omega_n = \sqrt{\frac{k}{m}}$, we get $\frac{c}{k} = \frac{\zeta 2\sqrt{km}}{k} = \frac{\zeta}{\pi f_n}$ and $\frac{c}{m} = \frac{2\zeta\sqrt{km}}{m} = 2\zeta\sqrt{\frac{k}{m}} = 4\pi\zeta f_n$. Here $2\pi f_n = \omega_n$. On substituting in the above equation, we get

$$\frac{\zeta}{R\pi f_n} \frac{d^3x}{dt^3} + \frac{d^2x}{dt^2} + 4\pi\zeta f_n \left(1 + \frac{3a}{kR} x^2 + \frac{1}{R} \right) \frac{dx}{dt} + 4\pi^2 f_n^2 x + 4\pi^2 f_n^2 \frac{a}{k} x^3 = \frac{F_{ext}}{m} + \frac{\zeta}{\pi f_n m R} \frac{dF_{ext}}{dt} \quad (\text{A.7})$$

To non-dimensionalize the above equation, the following non-dimensional variables are used:

$$x^* = \frac{x}{D}, t^* = \frac{Ut}{D}, f_n^* = \frac{Df_n}{U}, m^* = \frac{m}{\frac{\pi}{4}\rho D^2}. \quad (\text{A.8})$$

On substituting into the above equation, together with using fluid force, $C_L = \frac{F_{ext}}{(1/2)\rho DU^2}$ and $\lambda = \frac{D}{\sqrt{k/a}}$ or $\lambda^2 = \frac{aD^2}{k}$ gives

$$\begin{aligned} \frac{d^3x^*}{dt^{*3}} + \frac{R\pi f_n^*}{\zeta} \frac{d^2x^*}{dt^{*2}} + 4\pi^2 f_n^{*2} (1 + R + 3\lambda^2 x^{*2}) \frac{dx^*}{dt^*} + \frac{4\pi^3 R f_n^{*3}}{\zeta} x^* + \frac{4\pi^3 R f_n^{*3} \lambda^2}{\zeta} x^{*3} \\ = \frac{2R f_n^* C_L}{m^* \zeta} + \frac{2}{\pi m^*} \frac{dC_L}{dt^*}. \end{aligned} \quad (A.9)$$

Note: Here λ is the nonlinearity strength defined as the inverse of non-dimensional position at which the force produced by the linear spring is equal to force produced by nonlinearity (Mackowski and Williamson, 2013). For a hardening spring, $\lambda = D/\sqrt{k/a}$, while for a softening spring $\lambda = -D/\sqrt{-k/a}$. Hence, to account for both, λ^2 should be replaced by $|\lambda|\lambda$.

References

- Amabili, M., 2018. Nonlinear damping in large-amplitude vibrations: modelling and experiments. *Nonlinear Dynam.* 93 (1), 5–18.
- Amabili, M., 2019. Derivation of nonlinear damping from viscoelasticity in case of nonlinear vibrations. *Nonlinear Dynam.* 97 (3), 1785–1797.
- Badhrshah, R., Bhardwaj, R., Bhattacharya, A., 2019. Lock-in regimes for vortex-induced vibrations of a cylinder attached to a bistable spring. *J. Fluids Struct.* 91, 102697.
- Bao, Y., Huang, C., Zhou, D., Tu, J., Han, Z., 2012. Two-degree-of-freedom flow-induced vibrations on isolated and tandem cylinders with varying natural frequency ratios. *J. Fluids Struct.* 35, 50–75.
- Bearman, P.W., 1984. Vortex shedding from oscillating bluff bodies. *Annu. Rev. Fluid Mech.* 16 (1), 195–222.
- Bearman, P., 2011. Circular cylinder wakes and vortex-induced vibrations. *J. Fluids Struct.* 27 (5–6), 648–658.
- Brika, D., Laneville, A., 1993. Vortex-induced vibrations of a long flexible circular cylinder. *J. Fluid Mech.* 250, 481–508.
- Dai, H., Abdelkefi, A., Wang, L., 2017. Vortex-induced vibrations mitigation through a nonlinear energy sink. *Commun. Nonlinear Sci. Numer. Simul.* 42, 22–36.
- De Haan, Y., Sluimers, G., 2001. Standard linear solid model for dynamic and time dependent behaviour of building materials. *HERON* 46 (1), 2001.
- Findley, W.N., Davis, F.A., 2013. Creep and Relaxation of Nonlinear Viscoelastic Materials. Courier Corporation.
- Gammaitoni, L., Neri, I., Vocca, H., 2009. Nonlinear oscillators for vibration energy harvesting. *Appl. Phys. Lett.* 94 (16), 164102.
- Govardhan, R., Williamson, C., 2000. Modes of vortex formation and frequency response of a freely vibrating cylinder. *J. Fluid Mech.* 420, 85–130.
- Harne, R.L., Wang, K., 2013. A review of the recent research on vibration energy harvesting via bistable systems. *Smart Mater. Struct.* 22 (2), 023001.
- Hourigan, K., Thompson, M., Tan, B., 2001. Self-sustained oscillations in flows around long blunt plates. *J. Fluids Struct.* 15 (3–4), 387–398.
- Huynh, B., Tjahjowidodo, T., Zhong, Z., Wang, Y., Srikanth, N., 2015. Nonlinearly enhanced vortex induced vibrations for energy harvesting. In: 2015 IEEE International Conference on Advanced Intelligent Mechatronics (AIM). IEEE, pp. 91–96.
- Huynh, B.H., Tjahjowidodo, T., Zhong, Z.-W., Wang, Y., Srikanth, N., 2017. Numerical and experimental investigation of nonlinear vortex induced vibration energy converters. *J. Mech. Sci. Technol.* 31 (8), 3715–3726.
- Karniadakis, G.E., Israeli, M., Orszag, S.A., 1991. High-order splitting methods for the incompressible Navier-Stokes equations. *J. Comput. Phys.* 97 (2), 414–443.
- Karniadakis, G., Sherwin, S., 2013. Spectral/HP Element Methods for Computational Fluid Dynamics. Oxford University Press.
- Khalak, A., Williamson, C.H., 1999. Motions, forces and mode transitions in vortex-induced vibrations at low mass-damping. *J. Fluids Struct.* 13 (7–8), 813–851.
- Kovacic, I., Brennan, M.J., 2011. The Duffing Equation: Nonlinear Oscillators and their Behaviour. John Wiley & Sons.
- Lee, H., Hourigan, K., Thompson, M.C., 2013. Vortex-induced vibration of a neutrally buoyant tethered sphere. *J. Fluid Mech.* 719, 97–128.
- Lee, Y., Vakakis, A.F., Bergman, L., McFarland, D., Kerschen, G., Nucera, F., Tsakirtzis, S., Panagopoulos, P., 2008. Passive non-linear targeted energy transfer and its applications to vibration absorption: a review. *Proc. Inst. Mech. Eng. K: J. Multi-body Dyn.* 222 (2), 77–134.
- Leontini, J.S., Jacono, D.L., Thompson, M.C., 2011. A numerical study of an inline oscillating cylinder in a free stream. *J. Fluid Mech.* 688, 551–568.
- Leontini, J., Stewart, B., Thompson, M., Hourigan, K., 2006a. Wake state and energy transitions of an oscillating cylinder at low Reynolds number. *Phys. Fluids* 18 (6), 067101.
- Leontini, J., Thompson, M., Hourigan, K., 2006b. The beginning of branching behaviour of vortex-induced vibration during two-dimensional flow. *J. Fluids Struct.* 22 (6–7), 857–864.
- de Lima, A., da Cunha, B., da Silva, A., Rodovalho, L., 2018. Vortex-induced vibration analysis of viscoelastically mounted rigid circular cylinders in cross-flow at a moderate Reynolds number. *J. Vib. Control* 24 (13), 2688–2700.
- Mackowski, A., Williamson, C., 2013. An experimental investigation of vortex-induced vibration with nonlinear restoring forces. *Phys. Fluids* 25 (8), 087101.
- Mishra, R., Kulkarni, S.S., Bhardwaj, R., Thompson, M.C., 2019. Response of a linear viscoelastic splitter plate attached to a cylinder in laminar flow. *J. Fluids Struct.* 87, 284–301.
- Mishra, R., Soti, A., Bhardwaj, R., Kulkarni, S.S., Thompson, M.C., 2020. Transverse vortex-induced vibration of a circular cylinder on a viscoelastic support at low Reynolds number. *J. Fluids Struct.* 95, 102997.
- Parkinson, G., 1989. Phenomena and modelling of flow-induced vibrations of bluff bodies. *Prog. Aerosp. Sci.* 26 (2), 169–224.
- Sarpkaya, T., 1979. Vortex-induced oscillations: a selective review. *J. Appl. Mech.* 46 (2), 241–258.
- Sarpkaya, T., 2004. A critical review of the intrinsic nature of vortex-induced vibrations. *J. Fluids Struct.* 19 (4), 389–447.
- Sheard, G.J., Thompson, M.C., Hourigan, K., 2003. From spheres to circular cylinders: the stability and flow structures of bluff ring wakes. *J. Fluid Mech.* 492, 147–180.
- Soti, A.K., Thompson, M.C., Sheridan, J., Bhardwaj, R., 2017. Harnessing electrical power from vortex-induced vibration of a circular cylinder. *J. Fluids Struct.* 70, 360–373.
- Sumer, B., et al., 2006. Hydrodynamics Around Cylindrical Structures, Vol. 26. World scientific.
- Thompson, M., Hourigan, K., Sheridan, J., 1996. Three-dimensional instabilities in the wake of a circular cylinder. *Exp. Therm Fluid Sci.* 12 (2), 190–196.
- Wang, E., Xu, W., Gao, X., Liu, L., Xiao, Q., Ramesh, K., 2019. The effect of cubic stiffness nonlinearity on the vortex-induced vibration of a circular cylinder at low Reynolds numbers. *Ocean Eng.* 173, 12–27.
- Williamson, C., Govardhan, R., 2004. Vortex-induced vibrations. *Annu. Rev. Fluid Mech.* 36, 413–455.
- Williamson, C., Govardhan, R., 2008. A brief review of recent results in vortex-induced vibrations. *J. Wind Eng. Ind. Aerodyn.* 96 (6–7), 713–735.
- Williamson, C.H., Roshko, A., 1988. Vortex formation in the wake of an oscillating cylinder. *J. Fluids Struct.* 2 (4), 355–381.
- Wu, X., Ge, F., Hong, Y., 2012. A review of recent studies on vortex-induced vibrations of long slender cylinders. *J. Fluids Struct.* 28, 292–308.
- Zhao, M., 2013. Flow induced vibration of two rigidly coupled circular cylinders in tandem and side-by-side arrangements at a low Reynolds number of 150. *Phys. Fluids* 25 (12), 123601.